Size-Resolved Dust Direct Radiative Effect Efficiency Derived from Satellite Observations

Qianqian Song[1,2,*], Zhibo Zhang[1,2], Hongbin Yu[3], Jasper F. Kok[4], Claudia Di Biagio[5], Samuel Albani[6], Jianyu Zheng[1,2], Jiachen Ding[7]

1. Physics Department, UMBC, Baltimore, Maryland, USA
2. Goddard Earth Sciences Technology and Research II, UMBC, Baltimore, Maryland, USA
3. Climate and Radiation Laboratory, NASA Goddard Space Flight Center, Greenbelt, Maryland, USA
4. Department of Atmospheric and Oceanic Sciences, University of California, Los Angeles, CA 90095, USA
5. Université Paris Cité and Univ Paris Est Creteil, CNRS, LISA, F−75013 Paris, France
6. Department of Environmental and Earth Sciences, University of Milano–Bicocca, Milan, Italy
7. Department of Atmospheric Sciences, Texas A&M University, College Station, Texas, USA

*Correspondence to: Qianqian Song

Email: cd11735@umbc.edu

Deleted: de

Deleted: Université

Abstract

The role of mineral dust aerosol in global radiative energy budget is often quantified by the dust direct radiative effect (DRE). The dust DRE strongly depends on dust aerosol optical depth (DAOD), therefore, DRE efficiency (DREE=DRE/DAOD) is widely compared across different studies to eliminate difference due to the various dust load. Nevertheless, DREE is still influenced by the uncertainties associated with dust particle size distribution (PSD) and optical properties. In this study, we derive a global clear-sky *size-resolved* DREE dataset in both shortwave (SW) and longwave (LW) at top of the atmosphere (TOA) and surface based on satellite observations (i.e., satellite-retrieved dust extinction spatial and vertical distributions). In the DREE dataset, dust geometric diameter from 0.1μm to 100 μm is divided into 10 bins and the corresponding monthly mean DREE (with respect to DAOD at 532nm) for each size bin is derived by using the Rapid Radiative Transfer Model (RRTM). Three sets of state-of-the-art dust refractive indices (RI) and two sets of dust shape models (sphere vs. spheroid) are adopted to investigate the sensitivity of dust DREE to dust absorption and shape. As a result, the size-resolved dust DREE dataset contains globally distributed monthly mean dust DREE at TOA and surface for each of 10 size bins with 5° (longitude) × 2° (latitude) resolution as well as for each dust RI and shape combination. The size-resolved dust DREE dataset can be used to readily calculate global dust DRE for any DAOD and dust PSD, including the uncertainty in the DRE induced by dust microphysical properties (e.g., dust PSD, RI and shape). By calculating dust DRE based on DAOD climatology retrieved from different satellite sensors and based on different dust PSD, we find that uncertainty in the spatial pattern of DAOD induces more than 10% of the uncertainty in SW dust DRE at TOA. The observation-based dust PSD induces around 15%~20% uncertainty in dust DRE at TOA and in the atmosphere. The sensitivity assessments of dust DRE to dust RI and shape

further suggest that dust non-sphericity induces a negligible effect on dust DRE estimations, while dust RI turns out to be the most important factor in determining dust DRE, particularly in SW.

1 Introduction

Mineral dust is an important component of the atmospheric aerosol (Textor et al., 2006; Choobari et al., 2014). They can influence the radiative energy budget of the Earth-Atmosphere system directly through their interaction with both solar and thermal infrared radiation, which is known as the direct radiative effect (DRE) of dust. The DRE of dust consists of two components. In the solar shortwave (SW) spectral region, dust aerosols reflect a fraction of solar radiation back to the space which generally leads to a negative cooling effect at both top of the atmosphere (TOA) and surface (Tegen et al., 1996; Myhre et al., 2003). In the longwave (LW) thermal infrared region, dust aerosols trap the thermal radiation emitted from Earth's surface by absorption, which generally leads to a positive warming radiative effect at TOA and surface (Sokolik et al., 1998). In addition to DRE, dust can also influence the radiation and the hydrological cycles indirectly through serving as cloud condensation nuclei and ice nuclei and affecting cloud microphysical properties and cloud lifetime, known as indirect effects of dust (Twomey, 1977; Albrecht, 1989).

The dust DRE depends on many factors including primarily the atmospheric dust content, represented by its optical depth (DAOD), vertical distribution (especially important for LW DRE), and particles' physico-chemical properties that are the particle size distribution (PSD), complex refractive index (RI), and shape. Besides dust PSD, RI and shape, the dust DRE also depends on the atmospheric composition and structure, notably the atmospheric vertical profile of clouds, water vapor, and temperature, as well as surface properties (Yu et al., 2006). All of these properties vary in space and time and need to be characterized at the best possible spatio-temporal resolution in order to get realistic dust DRE estimates.

Among all these factors, DAOD is of first order importance in determining dust DRE since dust DRE is approximately linear with DAOD (Satheesh and Ramanathan, 2000). Many previous studies related to dust DRE are based on DAOD distributions from model simulations. For example, Kok et al. (2017) used four global model simulations to estimate global mean dust DRE efficiency (DREE is defined as DRE/DAOD) and further derive global mean dust DRE. Di Biagio et al. (2020) derived dust DRE based on model-simulated DAOD distributions with global annual mean DAOD constrained by observations. The main advantage of these studies is the availability of continuous and detailed DAOD spatial and temporal variation from model simulations. On the other hand, model-simulated DAOD could be subject to large uncertainties and biases in reproducing DAOD due to parameterizations of various physical processes, therefore need observational constraints for evaluation and improvement.

Satellite observations are important sources of data for evaluating model simulations, because of their routine sampling on a global scale and over decadal time periods. Previous studies have developed sensor-specific methods to distinguish dust aerosol from total aerosol based on the size and shape characteristics of dust particles. Some are based on passive satellite observations such as Moderate Resolution Imaging Spectroradiometer (MODIS, Remer et al. (2005)) and others are based on active observations such as Cloud-Aerosol Lidar with Orthogonal Polarization (CALIOP, Winker et al. (2009)). The wide spectral coverage of MODIS measurements allows the retrieval of aerosol particle size information, such as effective radius, fine-mode fraction, aerosol Angstrom exponent, as well as spectral gradient of absorption (Remer et al., 2005; Hsu et al., 2013). Based on the fact that dust aerosols are generally larger in size than other aerosols and have a decreasing absorption from ultraviolet (UV) to the near infrared, the combinations of these retrievals provide the basis for dust separation and dust aerosol optical depth (DAOD) retrievals from MODIS (Kaufman et al., 2005; Ginoux et al., 2012; Voss and Evan, 2020; Yu et al., 2009, 2019). In addition, some recent studies have also characterized dust distribution through integrating MODIS measurements with other data sources and model simulations, for example, using the DAOD-to-AOD ratio from MERRA-2 (Modern-Era Retrospective analysis for Research and Applications, version 2), Gkikas et al. (2021) converted the MODIS AOD retrievals to DAOD. However, passive sensors do not provide the vertical structure of aerosol that is critical for studying aerosol–cloud interactions, LW radiative effects and aerosol influences on the thermal structure of the atmosphere (e.g., Meloni et al., 2005, 2015). By contrast, the active sensor CALIOP can provide the vertical profiles of aerosol extinction and particle properties such as depolarization ratio and color ratio, which have been used for improving DAOD retrievals in thermal infrared (TIR) (Zheng et al., 2022) and evaluating global dust simulations (Yu et al., 2010; Wu et al., 2020). The CALIOP dust identification is mainly based on dust aerosols being non-spherical in shape and their linear depolarization ratio being much larger than spherical aerosols (Sakai et al., 2010).

Using CALIOP retrievals, Song et al. (2021) derived a three-dimensional (3D) decadal (2007-2019) global scale dust extinction profile climatology, which provides an observational constraint on both the spatial DAOD pattern and the vertical dust distribution for studying dust DRE and evaluating models. In their study, Song et al. (2021) also compared dust retrievals, in particular DAOD, based on different methods (i.e., CALIOP-based and MODIS-based DAOD retrievals), showed that DAOD often differ significantly between the different products and further discussed the potential reasons of causing the differences (e.g., instrument calibration errors and errors in discriminating cloud from aerosol, globally uniform dust Lidar Ratio assumption in CALIOP DAOD retrieval and so on). They showed that DAOD derived from CALIOP observations is generally smaller and more concentrated over ‘dust belt’ regions - extending from

Deleted: and

Deleted: . For example, they

the west coast of north Africa to the Middle East, central Asia, and China - than that derived from MODIS observations. These differences in DAOD in turn lead to different dust DRE estimations, making it difficult to compare different studies to reach meaningful conclusions. Even an agreement of DRE could be a result of the compensation between differences in DAOD and other aforementioned factors, such as dust microphysical properties. Therefore, DRE provides only a weak constraint on model. Instead, a normalized quantity, DRE efficiency (DREE) as the ratio of DRE to DAOD, has been widely used in inter-comparison studies and model evaluations (Di Biagio et al. 2020). Because of the elimination of DAOD, the DREE provides a stronger constraint on dust microphysical properties and their impacts on the dust DRE from different dust source regions (García et al., 2008).

In addition to DAOD, dust size is also an important factor in determining dust DRE (Mahowald et al., 2014). Smaller particles are more effective at scattering SW radiation and super-micron particles are more effective at absorbing both SW and LW radiation (Tegen and Lacis, 1996).Therefore, when other parameters are equal, fine dust would generally have a more negative SW DRE and a less positive LW DRE than coarse dust. Unfortunately, despite its importance, the simulation of dust PSD in the models and satellite retrievals of dust size remain challenging tasks (Ryder et al., 2019). As a result, there is a large uncertainty in our understanding of dust PSD. For example, several recent studies suggested that model simulations tend to underestimate dust size, especially the very coarse dust with diameter in excess of 5 μm (Adebiyi and Kok, 2020). Moreover, dust RI and shape can be important for DRE estimation as well because besides dust PSD they are the other two factors that determine dust spectral optical properties. As such, it is important to investigate the sensitivity of dust DRE to dust PSD, RI and shape. Previous studies suggest that large dust PSD and RI uncertainty leads to a large uncertainty in dust DRE and thereby

DREE estimations. For example, Song et al., (2018) shows that the SW DREE of a dust model with a large size and less absorptive RI is very similar to that of a dust model with a smaller size and more absorptive RI, both in the range of satellite derived values in the NE Atlantic region. Not surprisingly, even DREE cannot provide sufficient constraints due to this possible compensation of effects in the dust PSD and RI.

The main objective of this study is to derive a global clear-sky size-resolved dust DREE dataset based on satellite observations and demonstrate its usefulness in constraining, comparing, and understanding the dust DRE estimations. As explained below, the size-resolved DREE decomposes the DREE of dust into several size bins and therefore provide a way to take into account the effects of dust PSD explicitly. The sensitivity of dust DRE to dust RI and shape are also assessed in this study. Due to the inhomogeneous spatio-temporal distribution of those aforementioned factors, it is thus important to consider the spatio-temporal variation of dust DREE. Therefore, we organize the DREE dataset at 5° (longitude) $\times$ 2° (latitude) horizontal resolution and at monthly temporal resolution. To the best of our knowledge, this work presents the first such dataset based on retrieved dust properties (i.e., DAOD vertical and horizontal distributions) from satellite observations, although size-resolved DREE from model simulations have been used in previous studies. We will show that our size-resolved DREE can allow users to readily compute the DREE and DRE of dust based on any dust PSD (e.g., from model simulations, satellite retrievals or in-situ measurements). We will also carry out an inter-comparison of the global dust DRE estimations based on different dust PSD and compare the results with previous studies. With these functions, we expect that the size-resolved DREE will be a useful tool for both observational and modeling studies of dust DRE.

The rest of the paper is organized as follows. Section 2 provides a description of the data and models used in this study. Section 3 describes the methodology of deriving the size-resolved DREE dataset. In section 4, we describe a methodology of calculating the dust DRE with the size-resolved DREE dataset and its validation. In section 5, we compare the regional and global dust DRE estimations based on different DAOD, dust PSD and compare the results with previous studies. Section 6 provides a summary of the study along with the main conclusions.

2 Data and Models

2.1 Satellite-based DAOD climatology

We use CALIOP-based DAOD climatology and dust vertical distribution derived in Song et al. (2021) to derive a size-resolved dust DREE. The reason for choosing CALIOP-based DAOD climatology is discussed in detail in section 3.2. The CALIOP-based dust climatology dataset contains monthly mean DAOD and dust vertical extinction profile on a 5° (longitude) × 2° (latitude) spatial resolution grid for the period 2007-2019. The CALIOP-based DAOD and dust vertical distribution climatology from 2007 to 2010 are used to derive monthly mean size-resolved dust DREE dataset in this study. The selection of 4 years (2007-2010) for DREE calculations is based on several considerations. Firstly, the multi-year DREE calculations allow us to investigate the effect of interannual variations of atmospheric and surface properties to dust DRE. Secondly, this selection is consistent with Song et al. (2018), making it easier to compare our results with previous work. Thirdly, considering the computational efficiency, we do not extend the calculation to more years.

In addition to CALIOP-based DAOD climatology, we will use the MODIS-based DAOD climatology to investigate the sensitivity of dust DRE to DAOD spatial pattern in section 5.2. The MODIS-based DAOD climatology achieves global coverage on a 5° (longitude) × 2° (latitude) spatial resolution for the period 2003-2019 by combining the monthly mean Aqua MODIS over-ocean (Yu et al., 2020) and over-land (Pu and Ginoux, 2018) DAOD. In contrast to CALIOP-based DAOD climatology which is based on dust non-sphericity to separate dust aerosol from CALIOP total aerosol observations, MODIS-based DAOD retrieval is mainly based on dust large size to partition DAOD from MODIS total aerosol observations. The two sensor-specific dust partition methods result in different DAOD magnitude and spatial pattern retrievals.

Figure 1 shows annual mean DAOD from 2007 to 2010 based on CALIOP and MODIS observations. CALIOP-based and MODIS-based DAOD climatology differ in terms of both magnitude and spatial pattern. MODIS-based DAOD is generally larger than CALIOP-based DAOD. For example, the global ($60^{\circ}S-60^{\circ}N$) 4-year mean MODIS-based DAOD is 0.047, while CALIOP-based DAOD is 0.032. High DAOD are seen from both CALIOP-based and MODIS-based DAOD over the 'dust belt' regions, where large-scale dust activities occur persistently throughout the year. However, the CALIOP-based DAOD is rather low in some other regions that are known to be dusty in certain seasons, such as South America, Australia, and South Africa. In other words, the two satellite-based DAOD spatial pattern differs significantly with CALIOP-based DAOD more concentrated over 'dust belt' regions.

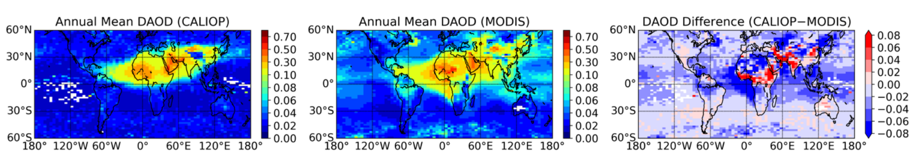

Figure 1. Global ($60^{\circ}S-60^{\circ}N$) spatial pattern of CALIOP-based and MODIS-based 4-year (2007-2010) mean DAOD (Song et al., 2021) and their difference.

Deleted: southwestern United States,

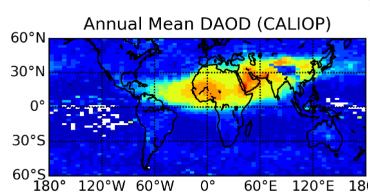

Deleted:

Deleted:).

2.2 Dust physical and optical models

To study the sensitivity of dust DREE to dust RI and dust shape, we adopt three sets of dust RI (Figure 2) and two dust shapes and compute a total of 6 sets of DREE based on their combinations. The three dust RI sets represent less absorptive, mean absorptive and more absorptive dust aerosols and the two dust shapes include spherical and spheroidal dust shapes (dust shape distribution is shown in Figure 4 (a) in Song et al. 2018). The mean, 10th and 90th percentile of calculated RI for 19 dust samples over 8 regions in Di Biagio et al. (2019) are used to represent mean, less and more absorptive dust in SW. We combine RI of wavelengths from 0.37μm to 0.95μm measured in Di Biagio et al. (2019) and RI of other wavelengths up to 3μm reported in Balkanski et al. (2007) to get full spectral coverage in SW. The mean, minimum and maximum RI of wavelengths beyond 3μm measured in Di Biagio et al. (2017) are used to represent mean, less and more absorptive dust in LW. Two dust shapes are used to investigate the effect of dust nonsphericity on dust DRE. One is spherical dust shape, the other one is spheroidal dust shape with dust aspect ratio distribution described by Figure 4 (a) in Song et al. (2018) which is originally from Dubovik et al. (2006). Each combination of dust RI and dust shape is considered as a dust model. As a result, the three dust RI and two dust shapes constitute six dust models in SW and LW, respectively, as shown in Table 1.

Deleted: (Figure 4 (a) in Song et al. 2018)

Deleted: .

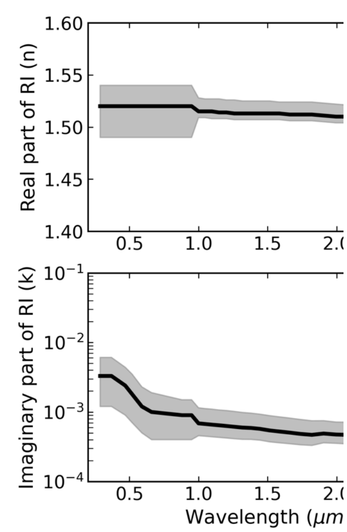

Deleted:

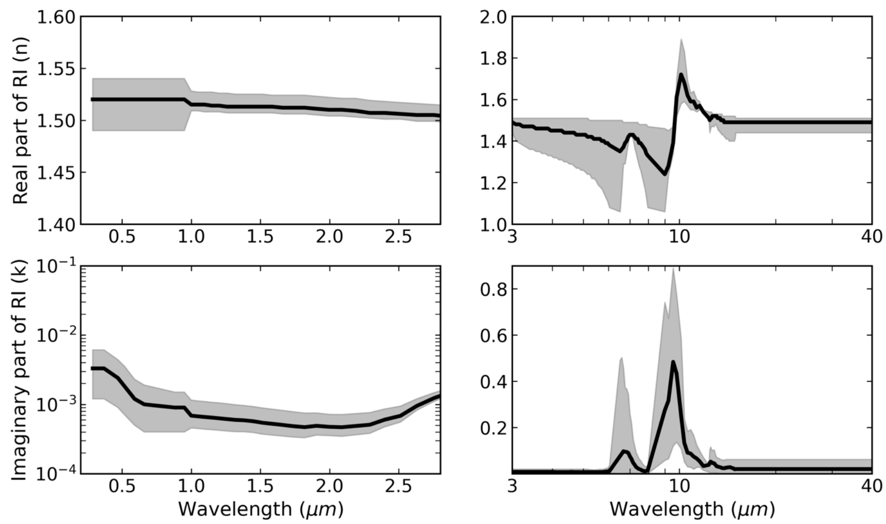

Figure 2. The SW and LW spectral refractive indices (RI) used in this study obtained from Di Biagio et al. (2017,2019) and Balkanski et al. (2007). The black curves represent the mean RI which indicates the mean absorptive dust. The grey shading represents the upper and lower limits indicating more absorptive and less absorptive dust, respectively.

Table 1. Dust models used in this study. Three dust RI are used in shortwave (SW) and longwave (LW) to represent less, mean, and more absorptive dust, respectively. Two dust shape models are used to represent spherical and spheroidal dust shape. The three dust RI sets and two dust shapes constitute 6 dust models in SW and LW respectively.

	SW RI (Balkanski et al. 2007; Di Biagio et al. 2019)			**LW RI** (Di Biagio et al. 2017)		
	10%	Mean	90%	Minimum	Mean	Maxmum
Sphere	MinSWRI-Sphere	MeanSWRI-Sphere	MaxSWRI-Sphere	MinLWRI-Sphere	MeanLWRI-Sphere	MaxLWRI-Sphere
Spheroid	MinSWRI-Spheroid	MeanSWRI-Spheroid	MaxSWRI-Spheroid	MinLWRI-Spheroid	MeanLWRI-Spheroid	MaxLWRI-Spheroid

3 Methodology

3.1 Size-resolved dust scattering properties

Rapid Radiative Transfer Model (RRTM) (Mlawer et al., 1997) is used to compute both SW and LW radiative fluxes for both clean (i.e., cloud-free and aerosol-free) and dusty atmospheres (i.e., free of clouds and non-dust aerosols). RRTM retains reasonable accuracy in

Deleted: .

Deleted: References for the used datasets are provided in Section 2.2.

comparison with line-by-line results for single column calculations (Mlawer and Clough, 1998; Mlawer et al., 1997). It divides the solar spectrum into 14 continuous bands ranging from 0.2 to 12.2 μm and the thermal infrared (3.08–1000 μm) into 16 bands. We explicitly specify the spectral DAOD, single scattering albedo (ω), and asymmetry parameter (g) of dust aerosols for every band in the RRTM radiative transfer simulations. In contrast to radiative transfer scheme in most global models, which do not account for LW scattering, scattering capability is available through the discrete-ordinate-method radiative transfer (DISORT) in RRTM_LW (Stamnes et al., 1988). Four streams are used in DISORT. The Henyey-Greenstein phase function is used and only the first moment of the phase function (i.e., asymmetry parameter) needs to be specified in the RRTM.

Dust scattering properties (extinction efficiency Qe, ω and g) depend on several factors including dust PSD, RI, and dust shape. To account for the impact of dust PSD, we divide dust diameters into 10 logarithmically spaced size bins. The 10 size bins represent a wide range of dust geometric diameters (i.e., diameter of a sphere with the same volume) ranging from $0.1\mu m$ to $100\mu m$. The geometric diameter (hereafter diameter or D) range of each size bin is listed in Figure 3. For each size bin k, the spectral scattering properties ($Qe_k^\lambda, \omega_k^\lambda$ and g_k^λ) are calculated for each dust model shown in Table 1 and each spectral band. In the calculations of scattering properties ($Qe_k^\lambda, \omega_k^\lambda$ and g_k^λ), dust particle number (dN/dD) is assumed to be uniformly distributed within each size bin. We use the Lorenz–Mie theory code of Wiscombe (1980) to compute the spectral optical properties of dust particles in the assumption of sphericity. The spectral optical properties of spheroidal dust particles are derived from the database of Meng et al. (2010). Figure 3 shows $Qe_k^\lambda, \omega_k^\lambda$ and g_k^λ for MeanSWRI-MeanLWRI-Spheroid dust model. In SW, finer dust has a larger ω and smaller g, implying a more effective SW backscattering of finer dust. As a result, finer dust is expected to have stronger cooling effect (more negative DREE values) at TOA generally. In

LW, $\frac{Qe_k^{10\mu m}}{Qe_k^{532nm}}$ is generally enhanced as dust size increases, which implies that coarser dust has larger extinction in LW (optically represented by $DAOD^{10\mu m}$) than finer dust when $DAOD^{532nm}$ is constrained by CALIOP retrieval. As a result, larger $DAOD^{10\mu m}$ will enhance the LW warming (more positive LW DREE) at TOA of coarser size bins. On the other hand, the increased ω *and* g of the coarser size bins indicates stronger forward scattering, which reduces the enhancement in LW warming induced by larger $DAOD^{10\mu m}$.

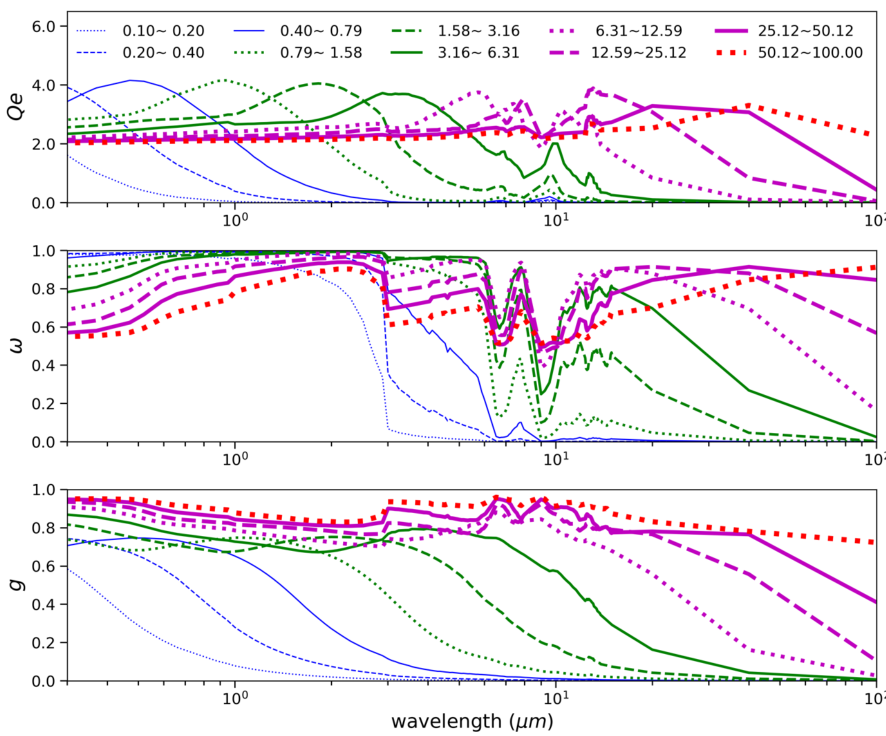

Figure 3. Spectral scattering properties (i.e., Q_e: extinction efficiency, ω: single scattering property, g: asymmetry parameter) of each size bin for the MeanSWRI-MeanLWRI-Spheroid dust model. The scattering properties of each size bin are represented by the corresponding curve indicated in the legend. Each size bin is defined with respect to dust diameter with unit of micrometers (μm).

3.2 DREE dataset

Based on the dust scattering properties shown in Figure 3 and the procedures summarized in Figure 4, we compute the size-resolved dust DREE for the MeanSWRI-MeanLWRI-Spheroid dust model in SW and LW. In this section, we focus on demonstrating the method of deriving size-resolved dust DREE for one dust model, but this method is applicable to all six dust models listed in Table 1.

First, we use RRTM to simulate monthly mean dust DRE from 2007 to 2010 for each 5° (longitude) × 2° (latitude) grid with CALIOP-based $DAOD^{532nm}$ exceeding 0.01. The $DAOD^{532nm}$>=0.01 threshold ensures most dusty regions over the globe are covered (see Figure S1 and Figure S2 in the Supplement) and in the meanwhile balances the computational cost. Dust DRE are calculated for each size bin using the extinction properties of the corresponding size bin shown in Figure 3 (denoted as $DRE_{k,i,j}$, hereafter k indicates size bin index and (i, j) indicates longitude-latitude grid index, unless specified otherwise). Note that we do not consider dust RI spatial variation and dust size vertical variation due to the lack of observation-based dust minerology and size estimation on global scale. In $DRE_{k,i,j}$ calculations, we constrain the monthly mean dust extinction vertical distributions using the CALIOP-based climatological dataset of Song et al. (2021). Worth to mention, our target in this section is $DREE_{k,i,j}$ calculations. Considering dust DRE is approximately linear to DAOD (Satheesh and Ramanathan, 2000), the DAOD used in dust DRE calculations will not affect dust DREE results significantly, we simply calculate dust $DRE_{k,i,j}$ with respect to $DAOD_{i,j}^{532nm}$ from CALIOP-based DAOD climatology. As a result, $DRE_{k,i,j}$ calculated in this section are only intermediate variables used to calculate dust DREE, they do not represent actual DRE contributed by k[th] size bin. The atmospheric profiles such as water vapor (H_2O), ozone (O_3) and temperature (T_{atm}) vertical profiles of 72 levels are from 3-

Deleted: Dust

Deleted: is calculated

hourly MERRA2 assimilated meteorological fields data (Gelaro et al., 2017). We combine the 1-hourly surface albedo for visible beam from MERRA2 radiation diagnostics with the instantaneous spectral surface albedo from the integrated CALIPSO, Cloud-Sat, CERES, and MODIS merged product (CCCM) (Kato et al., 2011) to get time-dependent spectral surface albedo. Surface temperature is obtained from 1-hourly MERRA2 radiation diagnostics data. The atmospheric and surface properties are all aggregated to monthly mean values at eight UTC times: 0:30, 3:30, 6:30, 9:30, 12:30, 15:30, 18:30, 21:30 to obtain monthly-mean diurnal cycle for radiative transfer simulations. Considering DRE^{SW} strongly depends on solar zenith angle (SZA), we calculate DRE^{SW} for every 1 hour using the corresponding hourly SZA in midmonth day. As a result, every three SZA share the same atmospheric and surface properties in DRE^{SW} calculations due to their different temporal resolution.

Table 2 List of definitions of variables and their indices.

Variable	Definition
k	size bin index
i, j	longitude-latitude grid index
t	8 UTC times with 3-hour interval (i.e., 0:30, 3:30, 6:30, 9:30, 12:30, 15:30, 18:30, 21:30)
tt	24 UTC times with 1-hour interval
day^{mm}	The midmonth day of the month
$\overline{R(t)}, \overline{H_2O(t)}, \overline{O_3(t)}, \overline{CO_2(t)}, \overline{T_{atm}(t)}$	3-hourly monthly mean surface albedo and vertical profile of water vapor, ozone, carbon dioxide and atmospheric temperature
ζ_d	dust properties such as DAOD, dust extinction vertical profile and scattering properties
$\overline{_{1h}DRE^{SW}_{k,i,j}(tt)}$	1-hourly monthly mean DRE^{SW} (i.e., monthly mean DRE^{SW} at each of 24 UTC times) of k^{th} size bin and (i^{th}, j^{th}) grid
$\overline{_{3h}DRE^{LW}_{k,i,j}(t)}$	3-hourly monthly mean DRE^{LW} (i.e., monthly mean DRE^{LW} at each of 8 UTC times) of k^{th} size bin and (i^{th}, j^{th}) grid
$\overline{DRE^{SW}_{k,i,j}}, \overline{DRE^{LW}_{k,i,j}}$	The monthly and diurnally mean dust DRE^{SW} and DRE^{LW} of k^{th} size bin and in (i^{th}, j^{th}) grid
$\overline{DREE_{k,i,j}}$	The monthly and diurnally mean dust $DREE^{SW}$ and $DREE^{LW}$ of k^{th} size bin and (i^{th}, j^{th}) grid
$\overline{DAOD^{532nm}_{i,j}}$	The monthly mean dust optical depth at 532nm of (i^{th}, j^{th}) grid

The definitions of variables and indices used to derive size-resolved dust DREE dataset are summarized in Table 2. Eq. (1) shows the way of deriving 1-hourly monthly mean DRE^{SW}.

$$\overline{{}_{1h}DRE^{SW}_{k,i,j}(tt)} = DRE^{SW}_{k,i,j}\left(\overline{R(t)}, \overline{H_2O(t)}, \overline{O_3(t)}, \overline{CO_2(t)}, \ \zeta_d, \ SZA(day^{mm}, tt)\right), \qquad (1)$$

where 't' indicates 8 UTC times with 3-hour interval. 'tt' indicates 24 UTC times with 1-hour interval. 'day^{mm}' indicates the midmonth day of the month, and '$\overline{R(t)}$' represents 3-hourly monthly mean surface albedo. We include 3-hourly monthly mean vertical profile of water vapor, ozone, carbon dioxide ($\overline{H_2O(t)}$, $\overline{O_3(t)}$, $\overline{CO_2(t)}$) to account for gaseous absorption. The temporal resolution inconsistency of SZA as well as atmospheric and surface properties requires every three SZA share the same atmospheric and surface properties in the calculations. 'ζ_d' represents dust properties such as DAOD, dust extinction vertical profile and scattering properties which are independent of UTC time in our calculations. Dust extinction vertical profile is interpolated to the 72 levels in consistency with vertical profiles of water vapor, ozone and temperature from MERRA2.

Eq. (2) shows the way of deriving 3-hourly monthly mean DRE^{LW}.

$$\overline{{}_{3h}DRE^{LW}_{k,i,j}(t)} = DRE^{LW}_{k,i,j}\left(\overline{E}, \overline{H_2O(t)}, \overline{O_3(t)}, \overline{CO_2(t)}, \overline{T_{atm}(t)}, \zeta_d\right) \qquad (2)$$

Surface spectral emissivity ('E') is obtained from Huang et al. (2016), which contains monthly mean spectral surface emissivity with 0.5-degree spatial resolution based on MODIS-retrieved mid-IR surface emissivity and modeled different types of surface spectral emissivity. $\overline{T_{atm}(t)}$ represents 3-hourly monthly mean vertical profile of atmospheric temperature. With the aid of the 3-hourly monthly mean atmospheric properties, monthly mean DRE^{LW} is calculated for every 3 hours.

$$\overline{{}_{3h}DRE^{LW}_{k,i,j}(t)} = DRE^{LW}_{k,i,j}\left(\overline{E}, \overline{H_2O(t)}, \overline{O_3(t)}, \overline{CO_2(t)}, \overline{T_{atm}(t)}, \zeta_d\right)$$

Then the 1-hourly monthly mean dust DRE^{SW} ($\overline{{}_{1h}DRE^{SW}_{k,i,j}(tt)}$) derived from Eq. (1) is averaged diurnally (over 24 points) to get the monthly and diurnally mean dust DRE^{SW} ($\overline{DRE^{SW}_{k,i,j}}$) as indicated by Eq. (3).

Moved down [1]: $\overline{O_3(t)}$, $\overline{CO_2(t)}$

Deleted: and

Moved (insertion) [1]

Moved (insertion) [2]

Deleted: .

Moved up [2]: ¶ $\overline{{}_{3h}DRE^{LW}_{k,i,j}(t)} = DRE^{LW}_{k,i,j}(\overline{E}, \overline{H_2O(t)}, \overline{O_3(t)}, \overline{CO_2(t)}, \overline{T_{atm}(t)}, \zeta_d)$

$$\overline{DRE^{SW}_{k,i,j}} = \frac{\sum_{tt} \overline{{}_{1h}DRE^{SW}_{k,i,j}(tt)}}{\sum tt} \tag{3}$$

Similarly, the 3-hourly monthly mean DRE^{LW} ($\overline{{}_{3h}DRE^{LW}_{k,i,j}(t)}$) derived from Eq. (2) is averaged diurnally (over 8 points) to get the monthly and diurnally mean dust DRE^{LW} ($\overline{DRE^{LW}_{k,i,j}}$) as indicated by Eq. (4).

$$\overline{DRE^{LW}_{k,i,j}} = \frac{\sum_{t} \overline{{}_{3h}DRE^{LW}_{k,i,j}(t)}}{\sum t} \tag{4}$$

The method described by Eq. (1) - Eq. (4) will be referred to as the '*conventional*' method of calculating monthly mean dust DRE in Section 4.

Based on the monthly mean size-resolved dust DRE^{SW} ($\overline{DRE^{SW}_{k,i,j}}$) and DRE^{LW} ($\overline{DRE^{LW}_{k,i,j}}$), we derive the monthly mean size-resolved dust DREE ($\overline{DREE_{k,i,j}}$) using Eq. (5) for SW and LW respectively. Note that the monthly mean size-resolved dust DREE ($\overline{DREE_{k,i,j}}$) is calculated by dividing by monthly mean $DAOD^{532nm}$ since the size-resolved $\overline{DRE_{k,i,j}}$ was initially derived with respect to monthly mean $DAOD^{532nm}$.

$$\overline{DREE^{SW\ or\ LW}_{k,i,j}} = \frac{\overline{DRE^{SW\ or\ LW}_{k,i,j}}}{\overline{DAOD^{532nm}_{i,j}}} \tag{5}$$

Finally, we average the monthly mean size-resolved dust DREE ($\overline{DREE_{k,i,j}}$) over 4 years to get monthly mean size-resolved dust DREE datasets in addition to the associated interannual standard deviation (std). The std indicates the DREE uncertainty caused by interannual variation of monthly mean atmospheric and surface properties as well as dust vertical distribution. Finally, the dataset developed in this study contains monthly mean size-resolved dust DREE and its associated interannual std at TOA and surface with dimension of 10 bins, 12 months, 90 latitudes,

Deleted: ¶
$\overline{DRE^{SW}_{k,i,j}} = \frac{\sum_{tt} \overline{{}_{1h}DRE^{SW}_{k,i,j}(tt)}}{\sum tt}$ ... [1]

72 longitudes for each of six dust models in SW and LW respectively. Figure S1 and Figure S2 in the Supplement demonstrate the global distribution of the monthly mean size-resolved $DREE^{SW}$ and $DREE^{LW}$ at TOA for June.

It is important to note that dust DREE of each grid cell rarely depends on the DAOD because dust DRE is approximately linear with DAOD (Satheesh and Ramanathan, 2000). Therefore, the choice of CALIOP- or MODIS-based DAOD climatology to derive the global (5° × 2°) size-resolved DREE dataset will not lead to large difference. In other words, the size-resolved DREE dataset is rarely related to the robustness of the DAOD used in the derivation process. We select CALIOP-based DAOD to derive the size-resolved dust DREE dataset because that the CALIOP-based dust climatology contains dust vertical distribution, which is especially important for obtaining LW DREE. Nevertheless, using CALIOP-based dust retrieval to derive size-resolved dust DREE dataset has several limitations: (1) The size-resolved dust DREE dataset may miss some regions with tenuous dust layers that below the CALIOP sensitivity. (2) The LW DREE is related to the quality of dust vertical distribution retrieval. By contrast, dust DRE highly depends on DAOD, therefore we will use different DAOD climatological datasets retrieved from different sensors (i.e., CALIOP and MODIS) to investigate global dust DRE in section 5.2. Furthermore, even though dust DREE of each grid cell is rarely related to DAOD, regional or global mean dust DREE will depend on the DAOD spatial distribution (i.e., DAOD 2D distribution) in the region of interest (see details in section 5.2).

Deleted: (Satheesh and Ramanathan, 2000)

Deleted: choose

Based on the monthly mean size-resolved dust DREE datasets derived above, we further calculate globally annual mean size-resolved dust $DREE^{SW}$ and $DREE^{LW}$ at TOA and surface for the six dust models (Figure 5). As discussed above, the global mean dust DREEs depends on the DAOD spatial distribution, the global mean dust DREEs shown in Figure 5 is based on CALIOP-based DAOD spatial distribution from Song et al. (2021). Generally smaller bins cause stronger cooling in SW and less warming in LW, which is consistent with our discussions in 3.1. This observationally informed globally annual mean size-resolved dust DREE is also consistent with the model-simulated results shown in supplementary Figure S3 in Kok et al. (2017) in terms of the variation trend of DREE with respect to dust size. Moreover, our study explicitly shows the sensitivity of dust DREE to dust RI and dust shape. For example, Figure 5 shows that $DREE^{SW}$ is strongly sensitive to dust RI as $DREE^{SW}$ of different dust RI is widely separated. Depending on dust RI, $DREE^{SW}$ switches from cooling effect (negative value) to warming effect (positive value) at different size bins. More absorptive dust starts to warm the Earth system in SW at smaller dust size, and vice versa. In addition, our results suggest that $DREE^{SW}$ is generally not sensitive to dust shape. Specifically, dust shape is not important for $DREE^{SW}$ in most size bins, while it is important in the fourth size bin ($D: 0.79\mu m \sim 1.58\mu m$) with $DREE^{SW}$ of spheroidal dust obviously higher (less negative) than spherical dust. In the $DREE^{LW}$, dust shape is almost as important as RI for several size bins.

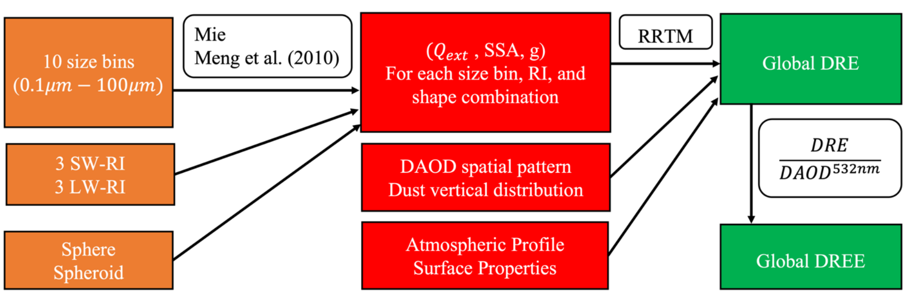

Figure 4. Schematic of the methodology used to derive size-resolved dust DREE dataset. Orange boxes denote dust models used to calculate dust scattering properties. Red boxes denote inputs for RRTM. Green boxes denote outputs from RRTM.

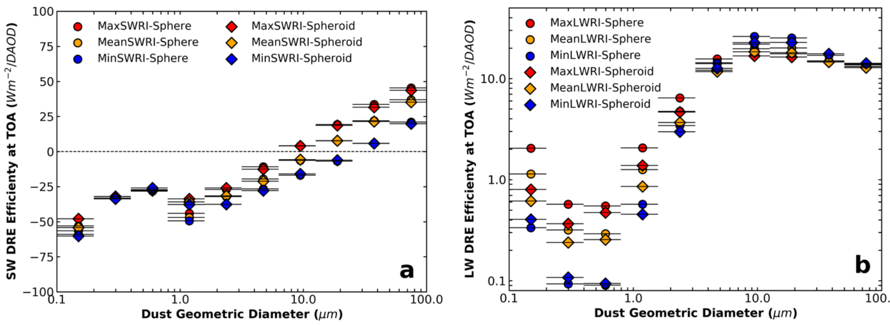

Figure 5. Globally annual mean size-resolved dust DREE in SW (**a**) and LW (**b**) for six dust models (six markers). Horizontal bars indicate the dust diameter range of each size bin. Note: LW DREE is on a logarithm scale; in contrast to global model simulations, we consider dust LW scattering in LW DRE Efficiency calculations.

Our size-resolved dust DREE dataset is unique in many aspects: First, our DREE dataset is derived based on CALIOP-based dust 3D distribution. Size-resolved DREE is derived for all grids with CALIOP-based DAOD >= 0.01. Second, our size-resolved DREE dataset covers a wide range of dust diameters, specifically, they include dust DREE for ten dust diameter size bins ranging from $0.1 \mu m$ to $100\ \mu m$. This is challenging, if not impossible, to obtain from global models because these models generally simulate dust particles with diameter only up to $20\ \mu m$ and coarse dust particles in models deposit quickly and could not be sustained to the remote transport regions (Huneeus et al., 2011; Adebiyi and Kok, 2020) where coarse particles have been observed by in-situ measurements (Weinzierl et al., 2017). As a result, our size-resolved DREE dataset achieves a wide spatial coverage for a large range of dust size. This is critical for investigating impacts of coarse dust and even giant dust particles on dust DRE on both regional and global scales. Third, considering that the dust vertical distribution is important for quantifying DRE^{LW}, we constrain dust vertical distribution using CALIOP-based dust retrievals in $DREE^{LW}$ computation. Fourth, our size-resolved dust DREE dataset accounts for dust LW scattering in $DREE^{LW}$ calculations since scattering capability is available through the DISORT in RRTM_LW (Stamnes et al., 1988). Dufresne et al., (2002) suggests that dust LW scattering enhances dust LW warming effect at TOA by a factor of up to 50%. However, dust LW scattering is generally not considered in most global models. Therefore, many previous studies artificially account for dust LW scattering by increasing the radiative perturbation due to LW absorption by a certain fraction. For example, Kok et al. (2017) accounts for LW scattering by artificially augmenting DRE^{LW} by 23% and Di Biagio et al. (2020) augmented DRE^{LW} by 50%.

On the other hand, our size-resolved dust DREE dataset has several limitations. First, possible vertical and horizontal variations of dust particle size in each grid box (5° × 2°) are not accounted for in our calculation. The entire dust-loading column in each grid box is assumed to have the same dust size distribution. Second, we do not explicitly account for spatial variation of dust RI, in other words, dust RI is assumed to be globally uniform. This uncertainty is assessed through the sensitivity tests of DREE to dust RI using three sets of state-of-the-art dust RI based on laboratory measurement of 19 dust samples all over the world. Third, dust 3D distribution in the DREE calculation is constrained by CALIOP observations. The limits on the sensitivity of CALIOP will affect the 3D distribution of dust in our calculation. Fourth, we account for dust nonsphericity by using spheroidal shape model. This shape can’t perfectly represent the highly irregular shape and roughness of real dust. In addition, several studies suggest that dust non-sphericity is underestimated by the spheroidal shape model (Huang et al., 2020). The spheroidal shape model assumption thus might produce systematic errors.

Deleted: in

Overall, the size-resolved dust DREE dataset is useful in many dust-related studies. First, with our size-resolved dust DREE dataset, dust DRE could be calculated efficiently for any DAOD magnitude, DAOD spatial pattern and any dust PSD for any regions or the globe (see details in Section 4.1). Second, our size-resolved DREE dataset is derived for different RI and different dust shapes respectively. As a result, we could estimate dust DRE uncertainty coming from DAOD, PSD, RI, and shape separately to better understand major uncertainty sources in dust DRE estimations. Third, our size-resolved DREE dataset could be used to evaluate model simulated DREE for each size bin.

4 DRE calculation methodology and its validation

4.1 DRE calculation based on DREE dataset

With the size-resolved dust DREE dataset derived in section 3.2, DRE of dust with any PSD and DAOD could be computed very efficiently without performing radiative transfer simulations as we do in *conventional* method. This section introduces the methodology of applying the size-resolved DREE dataset to calculate DRE of dust with any PSD and DAOD.

DRE of full-size range of dust can be expressed as the sum of DRE from each size bin (DRE_k). Dust DRE_k is approximated to be linearly proportional to DAOD of k^{th} size bin ($DAOD_k$) (Satheesh and Ramanathan, 2000). The similar concept of calculating dust DRE has been used in previous studies e.g., Kok et al. (2017). Eq. (6) shows the process of computing dust DRE using the size-resolved DREE dataset.

$$DRE = \sum_k DRE_k = \sum_k DREE_k \times DAOD_k = \sum_k DREE_k \times f_k \times DAOD, \quad (6)$$

where DRE represents dust DRE induced by full size range of dust with optical depth of $DAOD$. f_k is the fraction of the DAOD contributed by the k^{th} size bin.

Each variable in Eq. (6) can be obtained or derived from datasets developed in this study and other studies. For example, the size-resolved DREE dataset ($DREE_{k,i,j}$) derived in this study is essential for utilizing this efficient and novel DRE calculation method. DAOD can be obtained from CALIOP-based or MODIS-based DAOD climatological datasets (Song et al., 2021). f_k can be derived from dust extinction efficiency (Qe), the geometric cross-sectional area (A) and dust PSD (dN/dD) based on Eq. (7).

$$f_k \equiv \frac{DAOD_k}{DAOD} = \frac{\int_{D^{k-}}^{D^{k+}} Qe^{532nm}(D)A(D)\frac{dN}{dD}dD}{\int_0^{D^{max}} Qe^{532nm}(D)A(D)\frac{dN}{dD}dD} \quad (7)$$

Qe is defined according to $Qe \equiv \frac{\sigma_e}{A}$, where σ_e is extinction cross section, the geometric cross-sectional area of the particle (A) can be expressed as $A = \pi r^2$. Under the assumption of spherical dust particle, r is the radius. Under the assumption of spheroidal dust particle, Vouk (1948) shows that the average projected area of a convex body (e.g., spheroidal particle) is $A = \pi r^2$, where r is the radius of a surface area-equivalent sphere. The average is taken over all possible orientations in space, which is consistent with our assumption of randomly oriented dust particles in the atmosphere. $Qe^{532nm}(D)$ for the six dust models are shown in Figure 6 (a), they all converge to 2 as the dust diameter becomes much larger than the wavelength, which is consistent with the principle of geometric optics (van de Hulst, 1957). By contrast, $Q_e^{550nm}(D)$ of non-spherical dust in Kok et al. (2017) has a much larger value than spherical dust for dust $D \geq 1\mu m$ (see their Figure 1(b)). This discrepancy is probably due to the different Q_e definitions used in the two studies. Kok et al. (2017) defined Q_e as dust extinction per unit cross section of volume-equivalent sphere. Figure 6 (b) shows that f_k of a specific PSD is not sensitive to dust RI and dust shape, this is also suggested by the similar Qe^{532nm} v.s. geometric diameter (D) trends of the six dust models shown in Figure 6 (a). In contrast, f_4 (i.e., f_k for the fourth size bin with D ranging from $0.79\mu m\ to\ 1.58\mu m$) is more sensitive to dust shape than other size bins, this is in line with the larger difference in Qe^{532nm} with shape shown in Figure 6 (a).

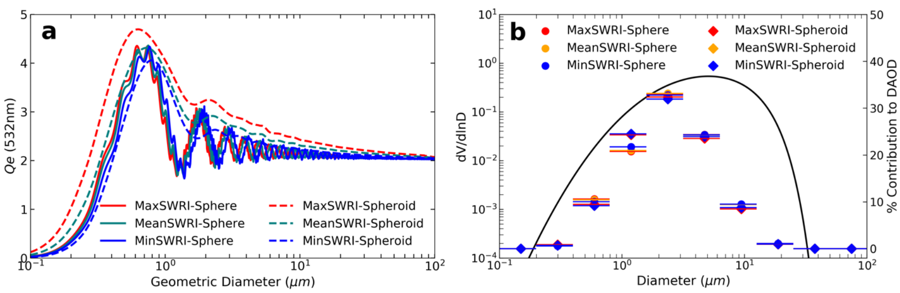

Figure 6. (**a**) Dust extinction efficiency (Qe) at 532nm for six dust models. (**b**) The colorful bars represent f_k calculated for six dust models based on a specific dust PSD ($dV/dlnD$) indicated by black curve. Note, f_k is not sensitive to different dust models such as dust RI and dust shape.

In summary, the size-resolved dust DREE dataset provides an efficient way to compute DRE for any dust PSD and any DAOD by using Eq. (6) and Eq. (7). To distinguish from the *conventional* method introduced in section 3.2, this method of calculating dust DRE based on size-resolved DREE dataset is referred to as '*DREE-integration'* method.

4.2 Validation of DRE calculation methodology

In this section, we select the Sahara Desert (14˚N-30˚N, 15˚W-30˚E) to validate the *DREE-integration* method. We choose MeanSWRI-MeanLWRI-Spheroid dust model and Fennec-Fresh dust PSD (see red curve in Figure 7) measured within 12h of dust uplift in remote Sahara locations by Fennec field campaign to represent microphysical properties of Saharan dust (Ryder et al., 2013a, b). Monthly mean DAOD is from CALIOP-based DAOD climatology.

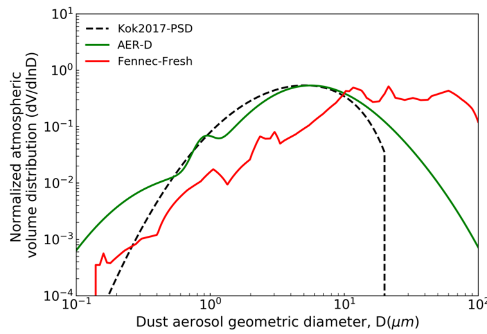

Figure 7. Normalized atmospheric dust volume distribution (dV/dlnD) described in Table 5 (Kok et al., 2017; Ryder et al., 2013a; b; 2018; 2019).

Figure 8 shows the comparison of 4-year (2007-2010) monthly mean dust DRE between the *Conventional* and *DREE-integration* method. In Conventional DRE calculation, dust scattering properties (Qe, ω and g) are calculated based on the Fennec-Fresh PSD and then used to calculate monthly mean dust DRE from 2007 to 2010 with RRTM as described in Section 3.2 (Eq. 1 – Eq. 4). While the DREE-integration method is based on the monthly mean size-resolved DREE dataset derived based on 4-year (2007-2010) data as described in Section 4.1 (Eq. 6 – Eq. 7). The excellent agreement in monthly mean dust DRE between two methods validates the *DREE-integration* DRE calculation methodology.

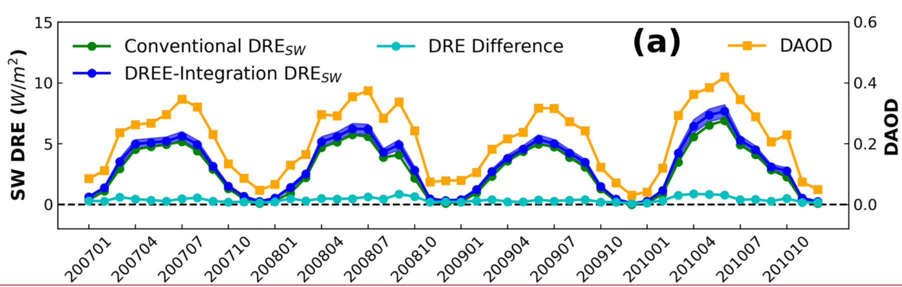

Deleted:

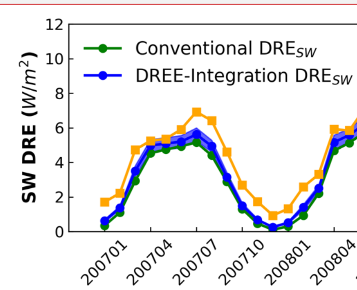

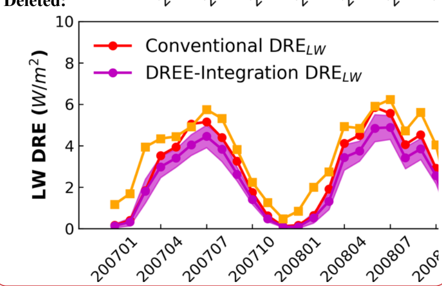

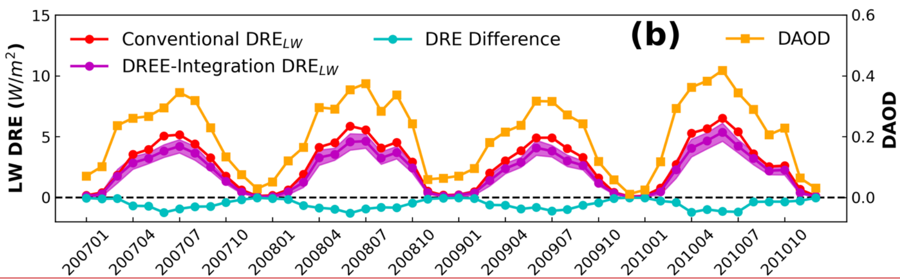

Figure 8. Monthly mean dust DRE^{SW} (**a**) and DRE^{LW} (**b**) comparison between *Conventional* and *DREE-integration* calculation from 2007 to 2010 over Sahara Desert. The DRE Difference line represents the difference between *DREE-integration* and Conventional calculation. Shaded area along *DREE-integration* DRE indicates the one standard deviation caused by the atmospheric and surface variations as well as dust vertical distribution variation within the four years. Orange curves indicate CALIOP-based monthly mean DAOD. The variation of dust DRE match well with DAOD variation.

The shaded-area associated with DREE-integration DRE corresponds to the one standard deviation of DREE caused by the 4-year (2007-2010) interannual variation of factors except dust microphysical properties such as monthly mean atmospheric and surface properties as well as dust vertical distributions (hereafter those factors is referred to as non-dust-factors for short). The narrow shaded-area along DREE-integration DRE suggests non-dust-factors cause very small uncertainty in dust DRE estimations. However, the small effects of 4-year interannual variation of non-dust-factors may not necessarily be representative due to the limited number of years considered. Section 2.1 discusses in detail for the reason of choosing 2007-2010 to derive size-resolved DREE dataset. To check the representative of 4-year interannual variation for non-dust-factors, we compare the 4-year (2007-2010) and 10-year (2007-2017) interannual standard deviation (std) of monthly mean non-dust-factors (e.g., surface albedo, surface temperature and dust vertical distribution) in Figure 9. To evaluate the interannual variation of dust vertical distribution, we define dust mean extinction height (Z_α) referring to Koffi et al. (2012) as $Z_\alpha = \frac{\sum_{i=1}^{n} \beta_{ext,i} \times Z_i}{\sum_{i=1}^{n} \beta_{ext,i}}$, where $\beta_{ext,i}$ is the dust extinction coefficient at 532nm at level *i,* and Z_i is the altitude of level *i*. Nevertheless the 10-year std is slightly larger than 4-year std, they are both close to zero and on the same order of magnitude. As such, even though our monthly mean size-resolved DREE dataset is derived from 4-year (2007-2010) data, they could be used to represent DREE and calculate DRE for other years considering the small sensitivity of monthly mean dust DRE to interannual variation of non-dust-factors.

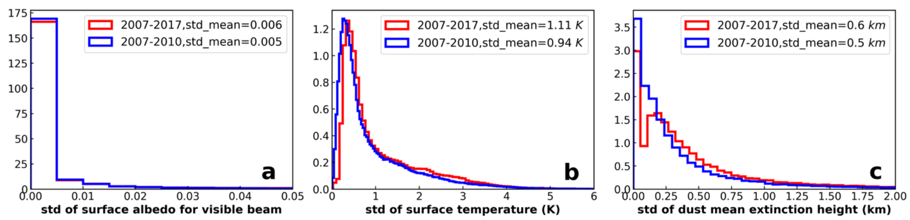

Figure 9. Probability density function (PDF) of 4-year and 10-year interannual standard deviation (std) in monthly mean (**a**) surface albedo, (**b**) surface temperature, and (**c**) dust mean extinction height. The PSD analyses include interannual std in 12 months and all 5° (longitude) × 2° (latitude) grid cells over the world and their mean values are indicated as 'std_mean' on each figure.

5 Regional and global dust DRE based on size-resolved DREE dataset

After the validation of *DREE-integration* method in Section 4, we use the *DREE-integration* method to calculate regional and global dust DRE in this section. There are three main objectives in this section: (1) the most important objective throughout this section is to demonstrate the usefulness of the size-resolved DREE dataset for calculating regional and global dust DRE for any given dust PSD; (2) the second objective is to validate the size-resolved DREE dataset by comparing with regional dust DREE reported by field studies based on satellite and ground-based observations (section 5.1); (3) the third objective to assess the sensitivity of dust DRE to DAOD spatial pattern (section 5.2) as well as dust microphysical properties such as dust PSD, RI and shape (section 5.3).

5.1 Comparison with observation-based regional dust DREE

Table 3 shows the comparison of our calculations of clear-sky regional mean SW and LW DREE with those reported by field studies based on satellite and ground-based observations. We first calculated regional mean dust DRE using the *DREE-integration* method, then divided by the corresponding regional mean DAOD to get regional mean DREE, and then compared this with observation-based results from previous studies. Comparing DREE allows eliminating differences due to the variation in regional dust loading, optically represented by DAOD.

Knowledge of regional dust PSD is necessary for estimating dust DRE regionally. There are several in-situ measurements of dust PSD over Sahara and tropical eastern Atlantic. The state-of-the art airborne observations of Saharan dust from the Fennec field campaign (Fennec-Fresh) and transported Saharan dust over tropical eastern Atlantic within Saharan Air Layer (SAL) from both AER-D and Fennec fieldwork campaigns are adopted (Ryder et al., 2013 a, b, 2018, 2019) (see Figure 7). Both campaigns include giant dust particles, measuring up to $100\mu m$ diameter for AER-D and up to $300\mu m$ for Fennec. The wide coverage of dust diameter in our size-resolved DREE dataset allows for dust DRE calculations for giant dust up to $100\mu m$ over both dust source and transported regions where giant particles are observed in those campaigns. This is an advantage of our size-resolved DREE dataset compared to modeled dust DREE, because climate models generally cut off dust diameter at 20 μm and could not sustain coarse dust to remote transport regions due to several missing mechanisms in models (Van Der Does et al., 2018; Drakaki et al., 2022; Meng et al., 2022).

The Fennec-Fresh dust PSD includes measurements within 12h of dust uplift in remote Sahara locations. It is used to calculate dust DRE for Saharan dust in this section. In reality, dust over the wide Sahara Desert region (15N~30N, 10W~30E) is not all lifted within 12h, so using

Fennec-Fresh to represent dust PSD over the wide Sahara Desert could bias dust size coarse, which could partially explain the warm bias in our $DREE^{SW}$ estimation over the Sahara Desert compared to the satellite-based result. Over the tropical Atlantic, both AER-D and Fennec-SAL measured PSD are used to assess the sensitivity of dust DREE to dust PSD. In addition, dust DRE is calculated for three dust RIs to evaluate the sensitivity of dust DREE to dust RI as shown in Table 3. Generally, our dust DREE estimations achieve good agreement with observation-based dust DREE. However, there is a significant uncertainty caused by dust RI in DREE, especially for SW. In addition, DRE comparisons between AER-D and Fennec-SAL over the Tropical Atlantic suggests that in-situ measured dust PSD uncertainty leads to a large uncertainty in regional DREE in both SW and LW.

Based on the regional DREE study with the state-of-the art RI and PSD, we found $DREE^{SW}$ uncertainty could come from both dust RI and dust PSD, while DRE^{LW} uncertainty is mainly from dust PSD.

Table 3. Comparison of our DREE estimations for different PSD and RI with Clear-Sky regional SW and LW dust DREE reported by field studies based on satellite and ground-based observations. Specifically, we calculated regional dust DREE for different RI (Min, Mean, Max) and different PSD (AER-D and Fennec-SAL for Tropical Atlantic) and then compare with observation-based results from previous studies. Note, spheroidal dust shape is assumed in our *DREE-integration* DRE calculations.

Shortwave Spectral Range							
Region	Season	Level	Satellite-Based	This study			
			$DREE^{SW}$	$DREE^{SW}$			PSD
				Min RI	Mean RI	Max RI	
Sahara Desert [a] (15N~30N, 10W~30E)	JJA	TOA	0	2.8	16.0	26.6	Fennec-Fresh
Ilorin[f], Nigeria (8.5N, 4.7E)	Annual	TOA	-15 ~ -35	-28.3	-24.1	-19.9	AER-D
				-23.4	-17.7	-12.9	Fennec-SAL
		Surface	-49 ~ -75	-43.1	-51.7	-59.3	AER-D
				-46.0	-57.1	-66.0	Fennec-SAL
Cape Verde[f] (16.7N, 22.9W)	Annual	TOA	-36 ~ -48	-42.3	-38.0	-33.7	AER-D
				-36.6	-30.8	-26.0	Fennec-SAL
		Surface	-68 ~ -90	-59.6	-68.7	-77.7	AER-D
				-61.5	-74.6	-85.3	Fennec-SAL
Tropical Atlantic [b] (10N~30N, 20W-45W)	JJA	TOA	-28	-44.6	-39.9	-35.3	AER-D
				-38.4	-32.1	-27.0	Fennec-SAL

		Surface	-82.1	-61.1	-71.9	-81.7	AER-D
				-64.4	-78.5	-90.0	Fennec-SAL
Tropical Atlantic [c] (15N~25N,15W~45W)	JJA	TOA	-35	-41.2	-36.3	-31.5	AER-D
				-35.1	-28.5	-23.1	Fennec-SAL
		Surface	-65	-57.9	-68.6	-78.1	AER-D
				-61.2	-75.1	-86.3	Fennec-SAL
Longwave Spectral Range							
Region	Season	Level	Satellite-Based	This study			
			DREE^{LW}	DREE^{LW}			PSD
				Min RI	Mean RI	Max RI	
Sahara Desert [a] (15N~30N, 10W~30E)	JJA	TOA	11~26	13.4	11.8	11.4	Fennec-Fresh
North Africa [d-e] (15N~35N, 18W~40E)	JJA	TOA	15~22	14.4	12.8	12.4	Fennec-Fresh
Tropical Atlantic [b] (10N~30N, 20W~45W)	JJA	TOA	10.5	8.2	8.1	8.5	AER-D
				13.1	11.8	11.6	Fennec-SAL
Cape Verde[g] (16.7N, 22.9W)	Sept	Surface	16	8.0	11.8	15.1	AER-D
				13.0	17.0	19.8	Fennec-SAL
(a) Patadia et al. (2009). (b) Song et al. (2018). (c) Li et al. (2004). (d) Zhang and Christopher (2003). (e) Brindley and Russell (2009). (f) Zhou et al. (2005). (g) Hansell et al. (2010)							

5.2 Global dust clear-sky DRE based on different DAOD climatology

The DAOD is the most important factor in determining dust DRE. As illustrated in Song et al. (2021), the DAOD retrieved from different satellite sensors have a large difference in terms of magnitude and spatial distribution. To evaluate how the current DAOD uncertainty affects dust DRE estimations, the global dust DRE computed based on monthly mean DAOD climatology retrieved from CALIOP observations and MODIS observations are compared in this section. To separate the effect of DAOD from other factors, we use the same dust PSD, RI and shape in the two sets of dust DRE calculations in this section. Specifically, we use the Fennec-Fresh PSD for three major dust source regions (i.e., Sahara (14-30°N, 15°W-30°E), Middle East (10-35°N, 40-85°E) and eastern Asia (30-50°N, 75-130°E), they are indicated by three black boxes in Figure 10) and use AER-D PSD for other regions (hereafter Campaign-PSD, see Table 5). The MeanSWRI-MeanLWRI-Spheroid dust model described in Table 1 is used to represent dust RI and shape.

The two DAOD climatological datasets result in distinct dust DRE spatial pattern as shown in Figure 10, which is consistent with the DAOD spatial patterns shown in Figure 1 suggesting CALIOP DAOD is more concentrated over 'dust belt' regions than MODIS DAOD. The global mean dust DRE^{SW}, DRE^{LW} and DRE^{NET} based on the two DAOD climatology are significantly different (Table 4), which is mainly caused by two factors. The first is the difference in DAOD magnitude. The CALIOP-based global mean DAOD is 0.032, while MODIS-based is 0.047. The other factor is the difference in DAOD spatial pattern. After we scale dust DRE to the same global mean DAOD ($\overline{DAOD} = 0.03$) to eliminate the effect of DAOD magnitude difference (values in parentheses in Table 4), the DRE^{SW} difference reduced from 0.55 W m^{-2} (-0.69 vs. -1.24 W m^{-2}) to 0.15 W m^{-2} (-0.64 vs. -0.79 W m^{-2}). Similarly, differences in DRE^{LW} and DRE^{NET} also reduce significantly. It indicates that the global mean DAOD magnitude difference is more important than the subtle difference in spatial pattern. Nevertheless, after scaling to the same global mean DAOD there is still more than 10% difference between the two dust DRE^{SW}, with CALIOP-based being the more positive one. This is probably because CALIOP-based DAOD is more concentrated over dust sources where dust aerosols induce less negative or even positive DRE^{SW} (For example the positive DRE^{SW} over the Sahara Desert and Arabia shown in Figure 10), which result in a less negative global mean DRE^{SW} than MODIS.

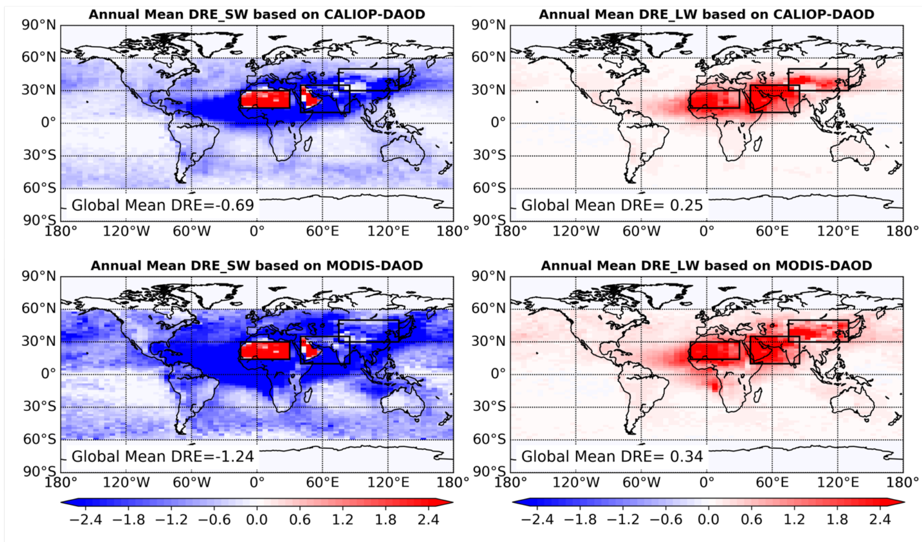

Figure 10. Annual mean dust DRE global distribution based on CALIOP-based and MODIS-based DAOD climatology. MeanSWRI-MeanLWRI-Spheroid dust model are used to represent dust RI and shape in the calculation. Campaign-PSD is used to represent dust PSD, specifically, Fennec-Fresh PSD is used to represent dust PSD over the three major dust source regions indicated by three black boxes. AER-D PSD is used to represent dust PSD over other regions.

Table 4. Globally annual mean DAOD, DRE^{SW}, DRE^{LW} and DRE^{NET} based on CALIOP DAOD and MODIS DAOD climatology. Note, values in the parentheses are for the two DAOD scaled to the same value of 0.03.

	$\overline{DAOD}$	$\overline{DRE^{SW}}$ [Wm^{-2}]	$\overline{DRE^{LW}}$ [Wm^{-2}]	$\overline{DRE^{NET}}$ [Wm^{-2}]
CALIOP	0.032 (0.03)	−0.69 (−0.64)	0.25 (0.23)	−0.44 (−0.41)
MODIS	0.047 (0.03)	−1.24 (−0.79)	0.34 (0.22)	−0.90 (−0.57)

5.3 Global dust clear-sky DRE based on different dust PSD

In the section 5.2, we showed the dust DRE based on the Campaign-PSD. As aforementioned, one of the main advantages of our size-resolved DREE is that it can be combined with different dust PSDs to estimate the dust DRE. To demonstrate this, we calculate another set of dust DRE based on the Kok2017-PSD. Table 5 describes the two dust PSDs used for global dust DRE calculations and their references. Kok2017-PSD is a globally averaged dust PSD and used to represent dust PSD for each dusty grid cell. It is constrained with observations and includes coarse dust particles up to $20 \mu m$. Although our primary goal here is to demonstrate the capability of our size-resolved DREE, the comparison between the two DRE can also help us understand the impacts of dust PSD uncertainty on the dust DRE estimation. Moreover, we also investigate the sensitivity of DRE to dust RI and dust shape explicitly in this section. The same DAOD climatology (CALIOP-based DAOD climatology) is used for dust DRE calculations to eliminate the impact of dust loading difference.

Several recent observation-constrained dust PSDs (e.g., Di Biagio et al., 2020, Adebiyi et al., 2020) suggest that dust size is coarser than Kok2017-PSD. As such, Kok2017-PSD is used to represent the lower limit of the observation-based global dust PSD to investigate the sensitivity of dust DRE to dust PSD. The Campaign-PSD is purely based on aircraft in-situ measurements and the aircraft was extensively equipped to measure giant particles with diameter larger than $20 \mu m$. We use the dust PSD measured over Sahara (from the Fennec field campaign) to represent dust PSD over three major dust source regions and use dust PSD measured in the Saharan Air Layer over the tropical eastern Atlantic (from AER-D field campaign) to represent dust PSD over dust transport regions. Of course, representing the spatial and temporal variation of global dust PSD with only two PSDs from the field campaigns is only a crude approximation due to the lack of PSD measurements. Dust aerosol over the three wide dust source regions may not be all uplifted within 12 hours as in the Fennec-Fresh measurements, in addition, dust size after long-range transport could be a bit finer than dust PSD measured over tropical eastern Atlantic (Weinzierl et al., 2017). Thus, Campaign-PSD likely represents the upper limit of the observation-based global dust PSD for the investigation of sensitivity to dust PSD. By contrast, the climate models miss most of coarse dust (D>5 μm) in the atmosphere (Adebiyi and Kok, 2020), as a result, the purely modeled dust PSD without observational constraints will lead to a substantially different dust DRE.

Deleted: spatially

Deleted: temporally

Therefore, the sensitivity test to dust PSD conducted in this study can only represent the uncertainty induced by the current understanding of observation-based dust PSD.

Table 5. The two observation-based dust PSDs used in DRE calculations (see Figure 7).

PSD	Description	Reference
Kok2017-PSD	A globally averaged atmospheric PSD derived from observation constrained globally averaged emitted PSD and model simulated globally averaged dust lifetime. This globally averaged PSD is used to represent dust PSD for each dusty grid cell. Dust diameter is cutoff at 20μm (Figure 2a in Kok et al.2017).	Kok et al. (2017)
Campaign-PSD	Fennec-Fresh PSD is used for three major dust source regions (i.e., Sahara (14-30°N, 15°W-30°E), Middle East (10-35°N, 40-85°E) and eastern Asia (30-50°N, 75-130°E)), which are indicated by the three black boxes in Figure 10. AER-D PSD is used for other regions.	Ryder et al. (2013a, b, 2018, 2019)

Deleted: Kok et al. (2017)

We calculated dust DRE of each grid cell ($DRE_{i,j}$) using *DREE-integration* method based on the dust PSD described in Table 5. Global mean dust DRE was then calculated by averaging dust $DRE_{i,j}$ weighted by its surface area. Figure 11 shows the global mean DRE^{SW}, DRE^{LW} and DRE^{NET} at TOA, surface, and in the atmosphere calculated based on the two sets of PSDs. Obviously, Kok2017-PSD leads to stronger cooling effect in SW and weaker warming effect in LW at TOA compared to Campaign-PSD, which is consistent with the fact that Kok2017-PSD is finer than the Campaign-PSD. In addition, we explicitly include the effects of dust RI and dust shape on DRE in Figure 11. Comparison of uncertainty induced by dust PSD, RI and shape suggests that dust RI uncertainty leads to the largest uncertainty in dust DRE, particularly RI uncertainty induces more than 40% uncertainty in DRE^{SW} estimations in the atmosphere (Figure 12). Dust PSD is also important for quantifying dust DRE, we found that the observation-based dust PSD uncertainty induces around 15%~20% uncertainty in dust DRE at TOA and in the atmosphere. Dust non-sphericity causes a negligible uncertainty in global mean dust DRE, in line with previous studies e.g., Raisanen et al. (2013) and Colarco et al. (2014).

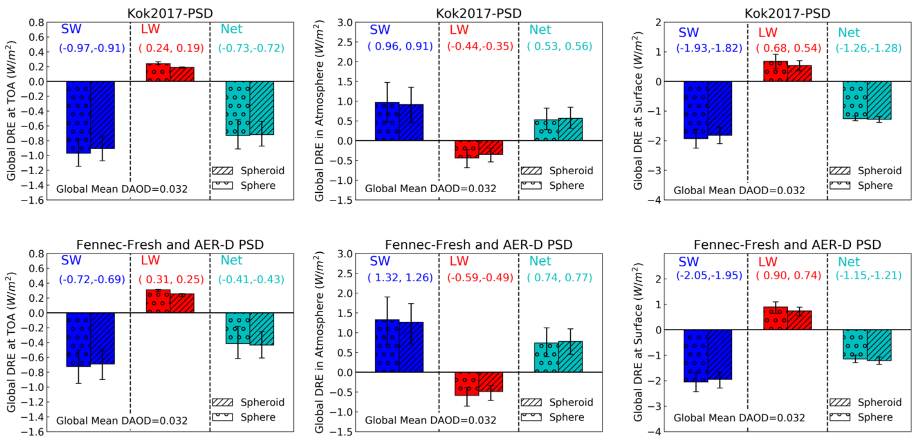

Figure 11. Globally annual mean clear-sky DRE^{SW}, DRE^{LW} and DRE^{NET} at TOA, in the atmosphere and surface calculated based on the two PSDs described in Table 5. The two rows represent dust DRE based on two PSDs. Error bars indicate uncertainty induced by dust RI uncertainty. Different types of bars indicate dust DRE based on different dust shapes. This figure explicitly separates the impacts of different dust microphysical properties on dust DRE. Two values in parenthesis on each plot represent spherical (left) and spheroidal (right) dust DRE corresponding to mean RI.

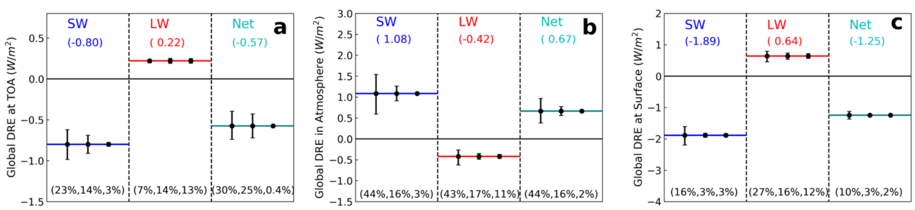

Figure 12. Comparison of uncertainty induced by dust RI, PSD and shape in DRE^{SW}, DRE^{LW} and DRE^{NET} at TOA (**a**), in the atmosphere (**b**) and surface (**c**). The horizontal lines in each plot represent global mean DRE^{SW} (blue line in the left column), DRE^{LW} (red line in the middle column) and DRE^{NET} (green line in the right column) averaged over two dust PSDs (i.e., Kok2017-PSD and Campaign-PSD) based on MeanRI-Spheroid dust model. The three error bars in each column represent DRE uncertainty induced by dust RI (left), dust PSD (middle) and dust shape (right). Accordingly, the percentage values on the bottom represent the percentage uncertainty induced by dust RI, PSD and shape, respectively.

It is tempting to compare our global mean dust DRE with results reported in Kok et al. (2017). But it must be noted that the global mean dust DRE shown in Figure 11 is for *clear sky* only, while the global mean dust DRE reported in Kok et al. (2017) is for *all sky*. The all-sky dust DRE can be separated into contributions from clear-sky and cloudy-sky portions (Myhre et al., 2020):

$$DRE_{all-sky} = (1 - CF) \times DRE_{clear-sky} + CF \times DRE_{cloudy-sky}, \quad (8)$$

where CF is cloud fraction, $DRE_{clear-sky}$ is dust DRE simulated under the case of removing all clouds, $DRE_{cloudy-sky}$ is the dust DRE assuming whole grid is covered by clouds. To compare our global mean dust DRE^{SW} based on Kok2017-PSD with the results reported in Kok et al. (2017), we convert our clear-sky $DRE^{SW}_{clear-sky}$ to $DRE^{SW}_{all-sky}$ by using MODIS L3 monthly mean cloud fraction. Specifically, we multiply $DRE^{SW}_{clear-sky}$ by (1-CF) for each grid cell and then calculate global annual mean values. In this process, we neglect the cloudy-sky dust DRE^{SW} portion because the annual mean cloudy-sky dust DRE^{SW} is estimated to be very small, around -0.04 (Zhang et al., 2016). Finally, our estimated global mean $DRE^{SW}_{all-sky}$ corresponding to DAOD=0.03 is around -0.34 Wm^{-2}. Although it is comparable to the -0.48 Wm^{-2} from Kok et al. 2017, the following differences between the two studies must be kept in mind when interpreting the results. First, the rough conversion from global mean $DRE^{SW}_{clear-sky}$ to global mean $DRE^{SW}_{all-sky}$ is subject to the approximation of global mean $DRE_{cloudy-sky} \sim 0$ and the MODIS L3 cloud fraction could be different from modeled cloud fraction used in Kok et al. (2017). Second, the two studies use different dust RI. For example, the imaginary part of RI at 550nm in this study ranges from 0.00061 to 0.003, while that in Kok et al. (2017) ranges from 0.0014 as used in GEOS-Chem and GISS model based on Sinyuk et al., (2003) to 0.003 as used in WRF-Chem based on Zhao et al., (2010). Third, in this study Kok2017-PSD is used to represent dust PSD in each dusty grid and applied to our size-resolved dust DREE dataset to calculate global dust DRE. In contrast, the model-simulated dust DREE in Kok et al. (2017) has reduced cooling from SW scattering and enhanced warming from SW absorption effects because the short lifetime of coarse dust in models concentrates these particles over bright deserts. Fourth, the two studies use different dust shape models, Kok et al. (2017) accounts for more nonspherical shape model (i.e., tri-axial ellipsoids).

Here we do not compare our global mean $DRE_{clear-sky}^{LW}$ with $DRE_{all-sky}^{LW}$ suggested in Kok et al. (2017) because that the lack of knowledge in $DRE_{cloudy-sky}^{LW}$ prevent us to convert $DRE_{clear-sky}^{LW}$ to $DRE_{all-sky}^{LW}$. Moreover, the two studies use different dust vertical profile, which is critical for DRE^{LW} estimations. For instance, dust vertical profile in Kok et al. (2017) is purely based on model simulations, while this study constrains dust vertical profile with CALIOP observations. Considering all these factors, it is hard to tell if the comparison is fair.

6 Summary and Conclusion

This study developed a clear-sky size-resolved dust DREE dataset in both SW and LW based on CALIOP-based dust DAOD climatology and dust vertical distributions. The dataset contains global monthly mean dust DREE at TOA and surface with 5° (longitude) × 2° (latitude) spatial resolution for 10 size bins ranging from $0.1\mu m$ to $100\mu m$ diameter, for three state-of-the art dust RI representing more, mean and less absorptive dust, and for two dust shapes representing spherical and spheroidal dust, respectively.

The size-resolved DREE dataset allows us to calculate dust DRE of any DAOD climatology and dust PSD efficiently by using the *DREE-integration* method presented in section 4.1 without involving radiative transfer simulations. The *DREE-integration* method is proven to be in great agreement with *conventional* DRE calculations. With the *DREE-integration* methodology, we firstly calculated clear-sky regional mean $DREE^{SW}$ and $DREE^{LW}$ over the Sahara Desert and tropical Atlantic. The comparison of our calculations with those reported by field studies based on satellite and ground-based observations shows reasonable agreement. Secondly, we estimated global mean dust DRE with two satellite-based DAOD climatological datasets and two different global dust PSDs. We found that the global mean DAOD magnitude difference between the two DAOD climatological datasets is more important than the subtle difference in spatial pattern. Nevertheless, after scaling to the same global mean DAOD there is still more than 10% difference between the two dust DRE^{SW}, with CALIOP-based being the more positive one. Moreover, our results explicitly show the uncertainty induced by each dust microphysical property (i.e., dust PSD, RI and shape) separately. When DAOD is constrained: (a) Dust non-sphericity induces negligible effect on dust DRE estimations; (b) The current understanding of observation-based dust PSD induces relatively large uncertainty (15%~20%) in dust DRE at TOA and in the atmosphere (c) Dust RI turns out to be the most important factor in determining dust DRE, particularly in SW. This implies that better understanding of dust mineral composition and RI will significantly improve our understanding in dust DRE in the future.

Data availability:

The size-resolved dust DREE dataset and the codes to calculate dust DRE for any given dust PSD and DAOD are available at 'https://drive.google.com/drive/folders/15_e28Y9JiSWiJnIM_2flEmt2u6i9phEY?usp=sharing'

CALIOP- and MODIS-based DAOD climatological datasets are available at 'https://drive.google.com/drive/folders/1aQVupe7govPwR6qmsqUbR4fJQsp1DBCX?usp=sharing'

Acknowledgement:

We would like to thank Dr. Claire L. Ryder for providing the Fennec and AER-D dust PSDs. Qianqian Song and Zhibo Zhang cordially acknowledge the funding support from the Future Investigators in NASA Earth and Space Science and Technology (FINESST). Zhibo Zhang's research is supported by NASA grant (80NSSC20K0130) from the CALIPSO and CloudSat program. S. Albani received funding from MIUR (Progetto Dipartimenti di Eccellenza 2018-2022).

The computations in this study were performed at the UMBC High Performance Computing Facility (HPCF). The facility is supported by the US National Science Foundation through the MRI program (grant nos. CNS-0821258 and CNS-1228778) and the SCREMS program (grant no. DMS-0821311), with substantial support from UMBC.

References

Adebiyi, A. A. and Kok, J. F.: Climate models miss most of the coarse dust in the atmosphere, Sci. Adv., 6, eaaz9507, https://doi.org/10.1126/sciadv.aaz9507, 2020.

Adebiyi, A. A., Kok, J. F., Wang, Y., Ito, A., Ridley, D. A., Nabat, P., and Zhao, C.: Dust Constraints from joint Observational-Modelling-experiMental analysis (DustCOMM): Comparison with measurements and model simulations, Atmos. Chem. Phys., 20, 829–863, https://doi.org/10.5194/acp-20-829-2020, 2020.

Albrecht, B. A.: Aerosols, Cloud Microphysics, and Fractional Cloudiness, Science (80-.)., 245, 1227–1230, https://doi.org/DOI 10.1126/science.245.4923.1227, 1989.

Balkanski, Y., Schulz, M., Claquin, T., and Guibert, S.: Reevaluation of Mineral aerosol radiative forcings suggests a better agreement with satellite and AERONET data, Atmos. Chem. Phys., 7, 81–95, https://doi.org/10.5194/acp-7-81-2007, 2007.

Di Biagio, C., Formenti, P., Balkanski, Y., Caponi, L., Cazaunau, M., Pangui, E., Journet, E., Nowak, S., Caquineau, S., Andreae O, M., Kandler, K., Saeed, T., Piketh, S., Seibert, D., Williams, E., and Doussin, J. F. C.: Global scale variability of the mineral dust long-wave refractive index: A new dataset of in situ measurements for climate modeling and remote sensing, Atmos. Chem. Phys., 17, 1901–1929, https://doi.org/10.5194/acp-17-1901-2017, 2017.

Di Biagio, C., Formenti, P., Balkanski, Y., Caponi, L., Cazaunau, M., Pangui, E., Journet, E., Nowak, S., Andreae, M. O., Kandler, K., Saeed, T., Piketh, S., Seibert, D., Williams, E., and Doussin, J. F.: Complex refractive indices and single-scattering albedo of global dust aerosols in the shortwave spectrum and relationship to size and iron content, Atmos. Chem. Phys., 19, 15503–15531, https://doi.org/10.5194/acp-19-15503-2019, 2019.

Di Biagio, C., Balkanski, Y., Albani, S., Boucher, O., and Formenti, P.: Direct Radiative Effect by Mineral Dust Aerosols Constrained by New Microphysical and Spectral Optical Data, Geophys. Res. Lett., 47, e2019GL086186, https://doi.org/doi:10.1029/2019GL086186, 2020.

Brindley, H. E. and Russell, J. E.: An assessment of Saharan dust loading and the corresponding cloud-free longwave direct radiative effect from geostationary satellite observations, J. Geophys. Res. Atmos., 114, https://doi.org/10.1029/2008JD011635, 2009.

Choobari, O. A., P. Zawar-Reza, and Sturman, A.: The global distribution of mineral dust and its impacts on the climate system: A review, Atmos. Res., 138, 152–165, https://doi.org/10.1016/j.atmosres.2013.11.007, 2014.

Colarco, P. R., Nowottnick, E. P., Randles, C. A., Yi, B. Q., Yang, P., Kim, K. M., Smith, J. A., and Bardeen, C. G.: Impact of radiatively interactive dust aerosols in the NASA GEOS-5 climate model: Sensitivity to dust particle shape and refractive index, J. Geophys. Res., 119, 753–786, https://doi.org/10.1002/2013jd020046, 2014.

Van Der Does, M., Knippertz, P., Zschenderlein, P., Harrison, R. G., and Stuut, J.-B. W.: The mysterious long-range transport of giant mineral dust particles, Sci. Adv., 4, 1–9, 2018.

Dubovik, O., Sinyuk, A., Lapyonok, T., Holben, B. N., Mishchenko, M., Yang, P., Eck, T. F., Volten, H., Munoz, O., Veihelmann, B., van der Zande, W. J., Leon, J. F., Sorokin, M., and Slutsker, I.: Application of spheroid models to account for aerosol particle nonsphericity in remote sensing of desert dust, J. Geophys. Res., 111, https://doi.org/Artn D11208 10.1029/2005jd006619, 2006.

Dufresne, J. L., Gautier, C., and Ricchiazzi, P.: Longwave scattering effects of mineral aerosols, J. Atmos. Sci., 59, 1959–1966, https://doi.org/10.1175/1520-0469(2002)059<1959:LSEOMA>2.0.CO;2, 2002.

García, O. E., Díez, A. M., Expósito, F. J., Díaz, J. P., Dubovik, O., Dubuisson, P., Roger, J. C., Eck, T. F., Sinyuk, A., Derimian, Y., Dutton, E. G., Schafer, J. S., Holben, B., and García, C. A.: Validation of AERONET estimates of atmospheric solar fluxes and aerosol radiative forcing by ground-based broadband measurements, J. Geophys. Res. Atmos., 113, https://doi.org/10.1029/2008JD010211, 2008.

Gelaro, R., McCarty, W., Suárez, M. J., Todling, R., Molod, A., Takacs, L., Randles, C. A., Darmenov, A., Bosilovich, M. G., Reichle, R., Wargan, K., Coy, L., Cullather, R., Draper, C., Akella, S., Buchard, V., Conaty, A., da Silva, A. M., Gu, W., Kim, G. K., Koster, R., Lucchesi, R., Merkova, D., Nielsen, J. E., Partyka, G., Pawson, S., Putman, W., Rienecker, M., Schubert, S. D., Sienkiewicz, M., and Zhao, B.: The modern-era retrospective analysis for research and applications, version 2 (MERRA-2), J. Clim., 30, 5419–5454, https://doi.org/10.1175/JCLI-D-16-0758.1, 2017.

Ginoux, P., Prospero, J. M., Gill, T. E., Hsu, N. C., and Zhao, M.: Global-scale attribution of anthropogenic and natural dust sources and their emission rates based on MODIS Deep Blue aerosol products, https://doi.org/10.1029/2012RG000388, 1 September 2012.

Gkikas, A., Proestakis, E., Amiridis, V., Kazadzis, S., Di Tomaso, E., Tsekeri, A., Marinou, E., Hatzianastassiou, N., and Pérez Garciá-Pando, C.: ModIs Dust AeroSol (MIDAS): A global fine-resolution dust optical depth data set, Atmos. Meas. Tech., 14, 309–334, https://doi.org/10.5194/amt-14-309-2021, 2021.

Hansell, R. A., Tsay, S. C., Ji, Q., Hsu, N. C., Jeong, M. J., Wang, S. H., Reid, J. S., Liou, K. N., and Ou, S. C.: An assessment of the surface longwave direct radiative effect of airborne Saharan dust during the NAMMA field campaign, J. Atmos. Sci., 67, 1048–1065, https://doi.org/10.1175/2009JAS3257.1, 2010.

Hsu, N. C., Jeong, M.-J., Bettenhausen, C., Sayer, A. M., Hansell, R., Seftor, C. S., Huang, J., and Tsay, S.-C.: Enhanced Deep Blue aerosol retrieval algorithm: The second generation, J. Geophys. Res. Atmos., 118, 9296–9315, https://doi.org/https://doi.org/10.1002/jgrd.50712, 2013.

Huang, Y., Kok, J. F., Kandler, K., Lindqvist, H., Nousiainen, T., Sakai, T., Adebiyi, A., and Jokinen, O.: Climate Models and Remote Sensing Retrievals Neglect Substantial Desert Dust Asphericity, Geophys. Res. Lett., 47, https://doi.org/10.1029/2019GL086592, 2020.

van de Hulst, H. C.: Light scattering by small particles, Wiley, Hoboken,NJ, 1957.

Huneeus, N., Schulz, M., Balkanski, Y., Griesfeller, J., Prospero, J., Kinne, S., Bauer, S., Boucher, O., Chin, M., Dentener, F., Diehl, T., Easter, R., Fillmore, D., Ghan, S., Ginoux, P., Grini, A., Horowitz, L., Koch, D., Krol, M. C., Landing, W., Liu, X., Mahowald, N., Miller, R., Morcrette, J. J., Myhre, G., Penner, J., Perlwitz, J., Stier, P., Takemura, T., and Zender, C. S.: Global dust model intercomparison in AeroCom phase i, Atmos. Chem. Phys., 11, 7781–7816, https://doi.org/10.5194/acp-11-7781-2011, 2011.

Kato, S., Rose, F. G., Sun-Mack, S., Miller, W. F., Chen, Y., Rutan, D. A., Stephens, G. L., Loeb, N. G., Minnis, P., Wielicki, B. A., Winker, D. M., Charlock, T. P., Stackhouse, P. W., Xu, K. M., and Collins, W. D.: Improvements of top-of-atmosphere and surface irradiance computations with CALIPSO-, CloudSat-, and MODIS-derived cloud and aerosol properties, J. Geophys. Res., 116, https://doi.org/Artn D19209 10.1029/2011jd016050, 2011.

Kaufman, Y. J., Koren, I., Remer, L. A., Tanré, D., Ginoux, P., and Fan, S.: Dust transport and deposition observed from the Terra-Moderate Resolution Imaging Spectroradiometer (MODIS) spacecraft over the Atlantic Ocean, J. Geophys. Res. D Atmos., 110, 1–16, https://doi.org/10.1029/2003JD004436, 2005.

Koffi, B., Schulz, M., Bréon, F. M., Griesfeller, J., Winker, D., Balkanski, Y., Bauer, S., Berntsen, T., Chin, M., Collins, W. D., Dentener, F., Diehl, T., Easter, R., Ghan, S., Ginoux, P., Gong, S., Horowitz, L. W., Iversen, T., Kirkevg, A., Koch, D., Krol, M., Myhre, G., Stier, P., and Takemura, T.: Application of the CALIOP layer product to evaluate the vertical distribution of aerosols estimated by global models: AeroCom phase i results, https://doi.org/10.1029/2011JD016858, 2012.

Kok, J. F., Ridley, D. A., Zhou, Q., Miller, R. L., Zhao, C., Heald, C. L., Ward, D. S., Albani, S., and Haustein, K.: Smaller desert dust cooling effect estimated from analysis of dust size and abundance, Nat. Geosci., 10, 274–278, https://doi.org/10.1038/Ngeo2912, 2017.

Li, F., Vogelmann, A. M., and Ramanathan, V.: Saharan dust aerosol radiative forcing measured from space, J. Clim., 17, 2558–2571, https://doi.org/Doi 10.1175/1520-0442(2004)017<2558:Sdarfm>2.0.Co;2, 2004.

Mahowald, N., Albani, S., Kok, J. F., Engelstaeder, S., Scanza, R., Ward, D. S., and Flanner, M. G.: The size distribution of desert dust aerosols and its impact on the Earth system, https://doi.org/10.1016/j.aeolia.2013.09.002, 1 December 2014.

Meloni, D., di Sarra, A., Di Iorio, T., and Fiocco, G.: Influence of the vertical profile of Saharan dust on the visible direct radiative forcing, J. Quant. Spectrosc. Radiat. Transf., 93, 397–413, https://doi.org/10.1016/j.jqsrt.2004.08.035, 2005.

Meloni, D., Junkermann, W., di Sarra, A., Cacciani, M., De Silvestri, L., Di Iorio, T., Estellés, V., Gómez-Amo, J. L., Pace, G., and Sferlazzo, D. M.: Altitude-resolved shortwave and longwave radiative effects of desert dust in the Mediterranean during the GAMARF campaign: Indications of a net daily cooling in the dust layer, J. Geophys. Res., 120, 3386–3407, https://doi.org/10.1002/2014JD022312, 2015.

Meng, Z. K., Yang, P., Kattawar, G. W., Bi, L., Liou, K. N., and Laszlo, I.: Single-scattering properties of tri-axial ellipsoidal mineral dust aerosols: A database for application to radiative transfer calculations, J. Aerosol Sci., 41, 501–512, https://doi.org/10.1016/j.jaerosci.2010.02.008, 2010.

Mlawer, E. J. and Clough, S. A.: Shortwave and longwave enhancements in the rapid radiative transfer model, Proc. Seventh Atmos. Radiat. Meas. Sci. Team Meet., 409–413, 1998.

Mlawer, E. J., Taubman, S. J., Brown, P. D., Iacono, M. J., and Clough, S. A.: Radiative transfer for inhomogeneous atmospheres: RRTM, a validated correlated-k model for the longwave, J. Geophys. Res. Atmos., 102, 16663–16682, https://doi.org/10.1029/97jd00237, 1997.

Myhre, G., Grini, A., Haywood, J. M., Stordal, F., Chatenet, B., Tanre, D., Sundet, J. K., and Isaksen, I. S. A.: Modeling the radiative impact of mineral dust during the Saharan Dust Experiment (SHADE) campaign, J. Geophys. Res., 108, https://doi.org/Artn 8579 10.1029/2002jd002566, 2003.

Myhre, G., Samset, B. H., Mohr, C. W., Alterskjær, K., Balkanski, Y., Bellouin, N., Chin, M., Haywood, J., Hodnebrog, O., Kinne, S., Lin, G., Lund, M. T., Penner, J. E., Schulz, M., Schutgens, N., Skeie, R. B., Stier, P., Takemura, T., and Zhang, K.: Cloudy-sky contributions to the direct aerosol effect, Atmos. Chem. Phys., 20, 8855–8865, https://doi.org/10.5194/acp-20-8855-2020, 2020.

Patadia, F., Yang, E. S., and Christopher, S. A.: Does dust change the clear sky top of atmosphere shortwave flux over high surface reflectance regions?, Geophys. Res. Lett., 36, https://doi.org/10.1029/2009GL039092, 2009.

Pu, B. and Ginoux, P.: How reliable are CMIP5 models in simulating dust optical depth?, Atmos. Chem. Phys., 18, 12491–12510, https://doi.org/10.5194/acp-18-12491-2018, 2018.

Raisanen, P., Haapanala, P., Chung, C. E., Kahnert, M., Makkonen, R., Tonttila, J., and

Nousiainen, T.: Impact of dust particle non-sphericity on climate simulations, Q. J. R. Meteorol. Soc., 139, 2222–2232, https://doi.org/10.1002/qj.2084, 2013.

Remer, L. A., Kaufman, Y. J., Tanré, D., Mattoo, S., Chu, D. A., Martins, J. V, Li, R. R., Ichoku, C., Levy, R. C., Kleidman, R. G., Eck, T. F., Vermote, E., and Holben, B. N.: The MODIS aerosol algorithm, products, and validation, J. Atmos. Sci., 62, 947–973, https://doi.org/10.1175/JAS3385.1, 2005.

Ryder, C. L., Highwood, E. J., Lai, T. M., Sodemann, H., and Marsham, J. H.: Impact of atmospheric transport on the evolution of microphysical and optical properties of Saharan dust, Geophys. Res. Lett., 40, 2433–2438, https://doi.org/10.1002/grl.50482, 2013a.

Ryder, C. L., Highwood, E. J., Rosenberg, P. D., Trembath, J., Brooke, J. K., Bart, M., Dean, A., Crosier, J., Dorsey, J., Brindley, H., Banks, J., Marsham, J. H., McQuaid, J. B., Sodemann, H., and Washington, R.: Optical properties of Saharan dust aerosol and contribution from the coarse mode as measured during the Fennec 2011 aircraft campaign, Atmos. Chem. Phys., 13, 303–325, https://doi.org/10.5194/acp-13-303-2013, 2013b.

Ryder, C. L., Marenco, F., Brooke, J. K., Estelles, V., Cotton, R., Formenti, P., McQuaid, J. B., Price, H. C., Liu, D., Ausset, P., Rosenberg, P. D., Taylor, J. W., Choularton, T., Bower, K., Coe, H., Gallagher, M., Crosier, J., Lloyd, G., Highwood, E. J., and Murray, B. J.: Coarse-mode mineral dust size distributions, composition and optical properties from AER-D aircraft measurements over the tropical eastern Atlantic, Atmos. Chem. Phys., 18, 17225–17257, https://doi.org/10.5194/acp-18-17225-2018, 2018.

Ryder, C. L., Highwood, E. J., Walser, A., Seibert, P., Philipp, A., and Weinzierl, B.: Coarse and Giant Particles are Ubiquitous in Saharan Dust Export Regions and are Radiatively Significant over the Sahara, Atmos. Chem. Phys. Discuss., https://doi.org/10.5194/acp-2019-421, 2019.

Sakai, T., Nagai, T., Zaizen, Y., and Mano, Y.: Backscattering linear depolarization ratio measurements of mineral, sea-salt, and ammonium sulfate particles simulated in a laboratory chamber, Appl. Opt., 49, 4441–4449, 2010.

Satheesh, S. K. and Ramanathan, V.: Large differences in tropical aerosol forcing at the top of the atmosphere and Earth's surface, Nature, 405, 60–63, https://doi.org/10.1038/35011039, 2000.

Sinyuk, A., Torres, O., and Dubovik, O.: Combined use of satellite and surface observations to infer the imaginary part of refractive index of Saharan dust, Geophys. Res. Lett., 30, https://doi.org/10.1029/2002GL016189, 2003.

Sokolik, I. N., Toon, O. B., and Bergstrom, R. W.: Modeling the radiative characteristics of airborne mineral aerosols at infrared wavelengths, J. Geophys. Res., 103, 8813–8826, https://doi.org/Doi 10.1029/98jd00049, 1998.

Song, Q., Zhang, Z., Yu, H., Kato, S., Yang, P., Colarco, P., Remer, L. A., and Ryder, C. L.: Net radiative effects of dust in the tropical North Atlantic based on integrated satellite observations and in situ measurements, Atmos. Chem. Phys., 18, https://doi.org/10.5194/acp-18-11303-2018, 2018.

Song, Q., Zhang, Z., Yu, H., Ginoux, P., and Shen, J.: Global dust optical depth climatology derived from CALIOP and MODIS aerosol retrievals on decadal timescales: regional and interannual variability, Atmos. Chem. Phys., 21, 13369–13395, https://doi.org/10.5194/acp-21-13369-2021, 2021.

Stamnes, K., Tsay, S.-C., Wiscombe, W., and Jayaweera, K.: Numerically stable algorithm for discrete-ordinate-method radiative transfer in multiple scattering and emitting layered media,

Appl. Opt., 27, 2502, https://doi.org/10.1364/ao.27.002502, 1988.
Tegen, I. and Lacis, A. A.: Modeling of particle size distribution and its influence on the radiative properties of mineral dust aerosol, J. Geophys. Res. Atmos., 101, 19237–19244, https://doi.org/10.1029/95jd03610, 1996.
Tegen, I., Lacis, A. A., and Fung, I.: The influence on climate forcing of mineral aerosols from disturbed soils, Nature, 380, 419–422, https://doi.org/10.1038/380419a0, 1996.
Textor, C., Schulz, M., Guibert, S., Kinne, S., Balkanski, Y., Bauer, S., Berntsen, T., Berglen, T., Boucher, O., Chin, M., Dentener, F., Diehl, T., Easter, R., Feichter, H., Fillmore, D., Ghan, S., Ginoux, P., Gong, S., Kristjansson, J. E., Krol, M., Lauer, A., Lamarque, J. F., Liu, X., Montanaro, V., Myhre, G., Penner, J., Pitari, G., Reddy, S., Seland, O., Stier, P., Takemura, T., and Tie, X.: Analysis and quantification of the diversities of aerosol life cycles within AeroCom, Atmos. Chem. Phys., 6, 1777–1813, 2006.
Twomey, S.: The influence of pollution on the shortwave albedo of clouds, J. Atmos. Sci., 34, 1149–1152, 1977.
Voss, K. K. and Evan, A. T.: A New Satellite-Based Global Climatology of Dust Aerosol Optical Depth, J. Appl. Meteorol. Climatol., 59, 83–102, https://doi.org/10.1175/JAMC-D-19, 2020.
Vouk, V.: Projected area of convex bodies [3], https://doi.org/10.1038/162330a0, 1948.
Weinzierl, B., Ansmann, A., Prospero, J. M., Althausen, D., Benker, N., Chouza, F., Dollner, M., Farrell, D., Fomba, W. K., Freudenthaler, V., Gasteiger, J., Gross, S., Haarig, M., Heinold, B., Kandler, K., Kristensen, T. B., Mayol-Bracero, O. L., Muller, T., Reitebuch, O., Sauer, D., Schafler, A., Schepanski, K., Spanu, A., Tegen, I., Toledano, C., and Walser, A.: THE SAHARAN AEROSOL LONG-RANGE TRANSPORT AND AEROSOL-CLOUD-INTERACTION EXPERIMENT Overview and Selected Highlights, Bull. Am. Meteorol. Soc., 98, 1427–1451, https://doi.org/10.1175/Bams-D-15-00142.1, 2017.
Winker, D. M., Vaughan, M. A., Omar, A., Hu, Y., Powell, K. A., Liu, Z., Hunt, W. H., and Young, S. A.: Overview of the CALIPSO mission and CALIOP data processing algorithms, J. Atmos. Ocean. Technol., 26, 2310–2323, https://doi.org/10.1175/2009JTECHA1281.1, 2009.
Wiscombe, W. J.: Improved Mie Scattering Algorithms, Appl. Opt., 19, 1505–1509, https://doi.org/Doi 10.1364/Ao.19.001505, 1980.
Wu, M., Liu, X., Yu, H., Wang, H., Shi, Y., Yang, K., Darmenov, A., Wu, C., Wang, Z., Luo, T., Feng, Y., and Ke, Z.: Understanding processes that control dust spatial distributions with global climate models and satellite observations, Atmos. Chem. Phys., 20, 13835–13855, https://doi.org/10.5194/acp-20-13835-2020, 2020.
Yu, H., Kaufman, Y. J., Chin, M., Feingold, G., Remer, L. A., Anderson, T. L., Balkanski, Y., Bellouin, N., Boucher, O., Christopher, S., DeCola, P., Kahn, R., Koch, D., Loeb, N., Reddy, M. S., Schulz, M., Takemura, T., and Zhou, M.: A review of measurement-based assessments of the aerosol direct radiative effect and forcing, Atmos. Chem. Phys., 6, 613–666, 2006.
Yu, H., Chin, M., Remer, L. A., Kleidman, R. G., Bellouin, N., Bian, H., and Diehl, T.: Variability of marine aerosol fine-mode fraction and estimates of anthropogenic aerosol component over cloud-free oceans from the Moderate Resolution Imaging Spectroradiometer (MODIS), J. Geophys. Res. Atmos., 114, https://doi.org/10.1029/2008JD010648, 2009.
Yu, H., Chin, M., Winker, D. M., Omar, A. H., Liu, Z., Kittaka, C., and Diehl, T.: Global view of aerosol vertical distributions from CALIPSO lidar measurements and GOCART simulations: Regional and seasonal variations, J. Geophys. Res. Atmos., 115, 1–19, https://doi.org/10.1029/2009JD013364, 2010.

Yu, H., Tan, Q., Chin, M., Remer, L. A., Kahn, R. A., Bian, H., Kim, D., Zhang, Z., Yuan, T., Omar, A. H., Winker, D. M., Levy, R. C., Kalashnikova, O., Crepeau, L., Capelle, V., and Chédin, A.: Estimates of African Dust Deposition Along the Trans-Atlantic Transit Using the Decadelong Record of Aerosol Measurements from CALIOP, MODIS, MISR, and IASI, J. Geophys. Res. Atmos., 124, 7975–7996, https://doi.org/10.1029/2019JD030574, 2019.

Yu, H., Yang, Y., Wang, H., Tan, Q., Chin, M., Levy, R., Remer, L., Smith, S., Yuan, T., and Shi, Y.: Interannual Variability and Trends of Combustion Aerosol and Dust in Major Continental Outflows Revealed by MODIS Retrievals and CAM5 Simulations During 2003–2017, Atmos. Chem. Phys. Discuss., 1–38, https://doi.org/10.5194/acp-2019-621, 2020.

Zhang, J. L. and Christopher, S. A.: Longwave radiative forcing of Saharan dust aerosols estimated from MODIS, MISR, and CERES observations on Terra, Geophys. Res. Lett., 30, https://doi.org/Artn 2188 10.1029/2003gl018479, 2003.

Zhang, Z. B., Meyer, K., Yu, H. B., Platnick, S., Colarco, P., Liu, Z. Y., and Oreopoulos, L.: Shortwave direct radiative effects of above-cloud aerosols over global oceans derived from 8 years of CALIOP and MODIS observations, Atmos. Chem. Phys., 16, 2877–2900, https://doi.org/10.5194/acp-16-2877-2016, 2016.

Zhao, C., Liu, X., Leung, L. R., Johnson, B., McFarlane, S. A., Gustafson, W. I., Fast, J. D., and Easter, R.: The spatial distribution of mineral dust and its shortwave radiative forcing over North Africa: Modeling sensitivities to dust emissions and aerosol size treatments, Atmos. Chem. Phys., 10, 8821–8838, https://doi.org/10.5194/acp-10-8821-2010, 2010.

Zheng, J., Zhang, Z., Garnier, A., Yu, H., Song, Q., Wang, C., Dubuisson, P., and Di Biagio, C.: The thermal infrared optical depth of mineral dust retrieved from integrated CALIOP and IIR observations, Remote Sens. Environ., 270, https://doi.org/10.1016/j.rse.2021.112841, 2022.

Zhou, M., Yu, H., Dickinson, R. E., Dubovik, O., and Holben, B. N.: A normalized description of the direct effect of key aerosol types on solar radiation as estimated from Aerosol Robotic Network aerosols and Moderate Resolution Imaging Spectroradiometer albedos, J. Geophys. Res. D Atmos., 110, 1–10, https://doi.org/10.1029/2005JD005909, 2005.

Page 18: [1] Deleted Qianqian Song 8/30/22 1:52:00 PM

Supplement of

Size-Resolved Dust Direct Radiative Effect Efficiency Derived from Satellite Observations

Qianqian Song et al.

Correspondence to: Qianqian Song (cd11735@umbc.edu)

1. Demonstration of monthly-mean *size-resolved* DREE dataset

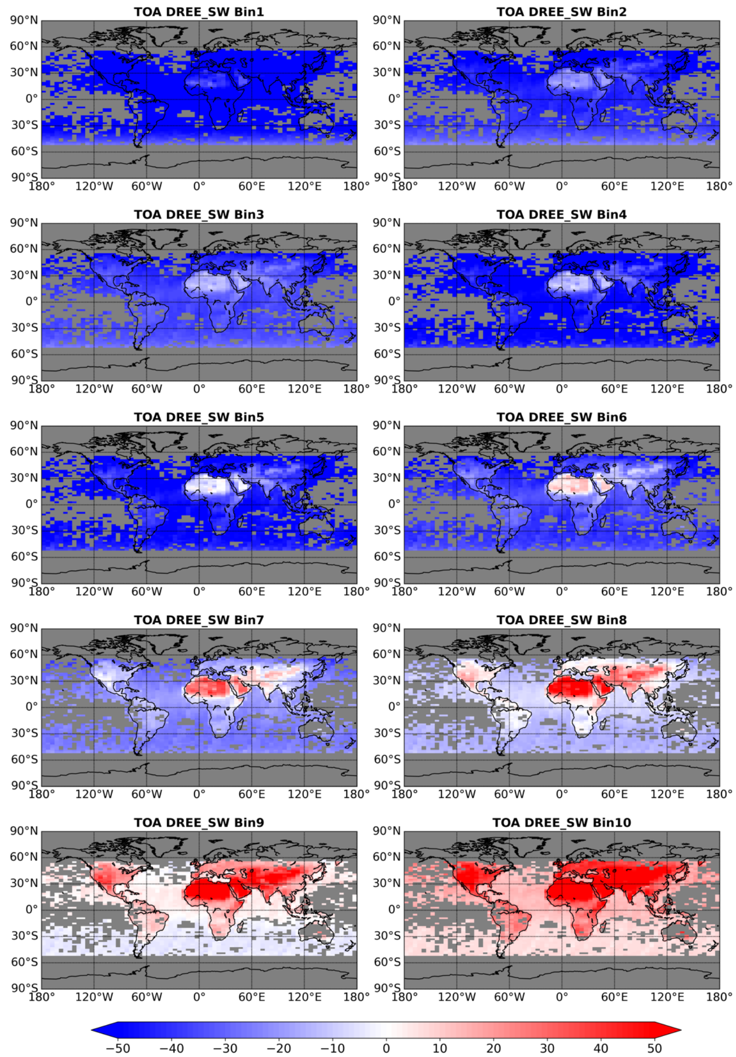

Figure S1. Global distribution of four-year (2007-2010) June monthly mean $DREE^{SW}$ of MeanSWRI-Spheroid dust model at TOA obtained from the *size-resolved* DREE dataset. Grey area indicates area without DREE derivations (e.g., DAOD retrieval is not available or $DAOD^{532nm}$ <=0.01 over the area).

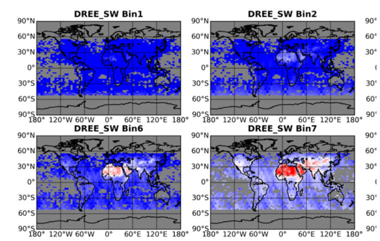

Deleted:

Deleted: -

Deleted: for June

Deleted: The strip pattern seen in large size bins (e.g., Bin7~Bin10) is due to the variation of surface albedo with SZA.…

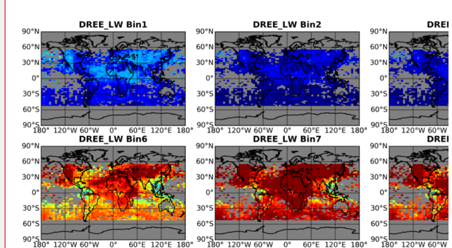

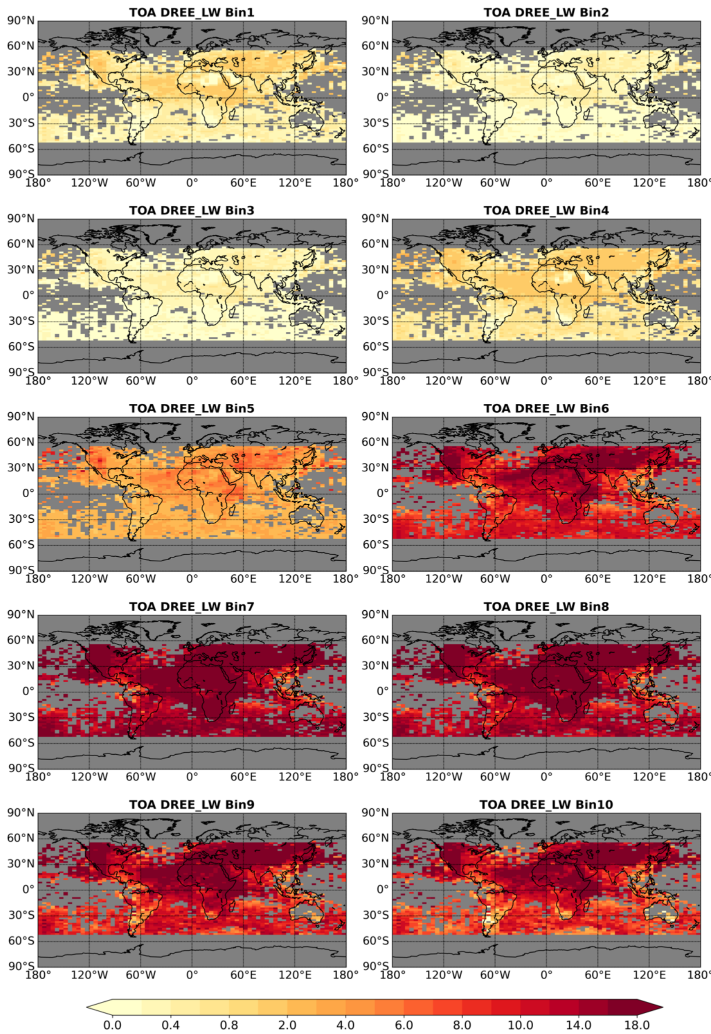

Figure S2. Global distribution of four-year (2007-2010) June monthly-mean DREE^{LW} of MeanLWRI-Spheroid dust model at TOA obtained from the *size-resolved* DREE dataset. Grey area indicates area without DREE derivations (e.g., DAOD retrieval is not available or $DAOD^{532nm}$ <=0.01 over the area).

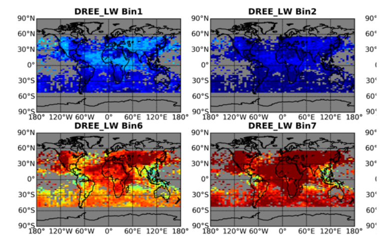

Deleted:

Deleted: for June